SANDIA REPORT

SAND2010-0044
Unlimited Release
Printed January 2010

Research on Micro-Sized Acoustic Bandgap Structures

Roy H. Olsson III, Ihab El-Kady, Mehmet F. Su, Melanie R. Tuck, Frederick B. McCormick and James G. Fleming

Prepared by
Sandia National Laboratories
Albuquerque, New Mexico 87185 and Livermore, California 94550

Sandia is a multiprogram laboratory operated by Sandia Corporation,
a Lockheed Martin Company, for the United States Department of Energy's
National Nuclear Security Administration under Contract DE-AC04-94AL85000.

Sandia National Laboratories

Issued by Sandia National Laboratories, operated for the United States Department of Energy by Sandia Corporation.

Available to DOE and DOE contractors from
U.S. Department of Energy
Office of Scientific and Technical Information
P.O. Box 62
Oak Ridge, TN 37831

Telephone: (865) 576-8401
Facsimile: (865) 576-5728
E-Mail: reports@adonis.osti.gov
Online ordering: http://www.osti.gov/bridge

Available to the public from
U.S. Department of Commerce
National Technical Information Service
5285 Port Royal Rd.
Springfield, VA 22161

Telephone: (800) 553-6847
Facsimile: (703) 605-6900
E-Mail: orders@ntis.fedworld.gov
Online order: http://www.ntis.gov/help/ordermethods.asp?loc=7-4-0#online

SAND2010-0044
Unlimited Release
Printed January 2010

Research on Micro-Sized Acoustic Bandgap Structures
(LDRD Project 105873)

Roy H. Olsson III and James G. Fleming
Advanced MEMS, Dept. 1749

Ihab El-Kady and Mehmet F. Su
Photonic Microsystems Technology, 1725

Melanie R. Tuck
MESAFAB Operations, Dept. 1746

Frederick B. McCormick
Applied Photonic Microsystems, Dept. 1727

Sandia National Laboratories
P.O. Box 5800
Albuquerque, New Mexico 87185

Abstract

Phononic crystals (or acoustic crystals) are the acoustic wave analogue of photonic crystals. Here a periodic array of scattering inclusions located in a homogeneous host material forbids certain ranges of acoustic frequencies from existence within the crystal, thus creating what are known as acoustic (or phononic) bandgaps. The vast majority of phononic crystal devices reported prior to this LDRD were constructed by hand assembling scattering inclusions in a lossy viscoelastic medium, predominantly air, water or epoxy, resulting in large structures limited to frequencies below 1 MHz. Under this LDRD, phononic crystals and devices were scaled to very (VHF: 30-300 MHz) and ultra (UHF: 300-3000 MHz) high frequencies utilizing finite difference time domain (FDTD) modeling, microfabrication and micromachining technologies. This LDRD developed key breakthroughs in the areas of micro-phononic crystals including physical origins of phononic crystals, advanced FDTD modeling and design techniques, material considerations, microfabrication processes, characterization methods and device structures. Micro-phononic crystal devices realized in low-loss solid materials were emphasized in this work due to their potential applications in radio frequency communications and acoustic imaging for medical ultrasound and nondestructive testing. The results of the advanced modeling, fabrication and integrated transducer designs were that this LDRD produced the 1st measured phononic crystals and phononic crystal devices (waveguides) operating in the VHF (67 MHz) and UHF (937 MHz) frequency bands and established Sandia as a world leader in the area of micro-phononic crystals.

Acknowledgements

The authors would like to acknowledge the memory of our late colleague and friend Jim Fleming. It was Jim's vision to pursue a research program in the area of acoustic bandgap crystals and his vision lives on today through the team he assembled. The authors would like that thank the MDL staff at Sandia National Laboratories including Jim Stevens for his work developing the AlN transducer film, Craig Nakakura for his work on AlN etching, Keith Yoneshige for his work supporting the tungsten chemical mechanical polish (CMP) and Todd Bauer and Rob Jarecki for their work on process and etch development. This project, Research on Micro-Sized Acoustic Bandgap Structures, LDRD Project 105873, was supported by Laboratory Directed Research and Development, Sandia National Laboratories, U.S. Department of Energy, under contract DE-AC04-94AL85000.

Table of Contents

List of Figures……………………………………………………………………..5

1 INTRODUCTION..11
2 MICRO-PHONONIC CRYSTAL DESIGN AND ANALYSIS 12
3 MICRO-PHONONIC CRYSTAL MATERIAL CONSIDERATIONS 17
  3.1 Air/solid phononic crystals...17
  3.2 Solid/solid phononic crystals...18
4 MICRO-SCALE PHONONIC CRYSTAL MODELING 19
5 MICRO-SCALE PHONONIC CRYSTAL FABRICATION 22
  5.1 VHF Phononic Crystal Fabrication...22
  5.2 UHF Phononic Crystal Fabrication...23
6 PHONONIC CRYSTAL DEVICE OPERATION AND MEASURED PERFORMANCE 23
  6.1 VHF Phononic Crystal Devices..23
  6.2 UHF Phononic Crystal Devices..29
7 APPLICATIONS...34
  7.1 Acoustic Isolators 34
  7.2 Phononic Crystal Waveguides...35
  7.3 Phononic Crystal Cavities and Filters...36
8 CONCLUSIONS 38
9 METRICS 39
10 REFERENCES...40

List of Figures

Figure 1. Schematic diagram of a 2D square lattice periodic crystal showing the distinct *ΓX* and *ΓM* directions of acoustic propagation inside the crystal, the lattice pitch, *a*, the lattice filling fraction, *r/a*, and the Bragg and Mie resonance conditions necessary for realizing a spectral bandgap. 14
Figure 2. Plot of the phononic crystal filling fraction, *r/a*, that sets the Mie and Bragg resonance conditions shown in figure 1 equal vs. the velocity mismatch between the matrix and scattering inclusion, V_M/V_i. While it is not necessary to set these resonances exactly equal, in order for the Mie resonance to contribute to a phononic bandgap, the width of the Bragg and Mie resonances must overlap which places limits on the desired velocity mismatch between the matrix and inclusion materials in a phononic crystal. 15
Figure 3. A representation of FDTD simulations of phononic crystals with finite thickness. PnC slab is surrounded with air buffers terminated by periodic boundary conditions in the x-axis, periodic boundary conditions terminating the phononic crystal in the y-axis and matrix material (SiO_2) covered Mur absorbers in the z-axis. 19
Figure 4. Normalized transmission (dB) vs. frequency (MHz) results for finite-thickness slabs with thicknesses (a) 0.25*a* (b) 0.5*a* (c) *a* (d) 1.5*a* (e) 5*a* (f) 10*a* (g) 25*a* (h) 50*a* where *a* is the lattice periodicity. Blue continuous lines belong to finite-thickness slabs; black dotted lines are infinite-thickness structure result for reference. 21
Figure 5. Micro-ABG process flow. 23
Figure 6. Micro-ABG slab with integrated AlN electro-acoustic couplers. The ABG is realized by including W scatterers in an oxide matrix. Acoustic frequencies within the gap can not pass between the AlN couplers. Inset shows close up image of the W scatterers and release holes. The lattice constant, *a*, is 45µm and *r* is 14.4 µm, yielding a volume filling fraction of 0.32. The release holes in the center of the W inclusions have a radius of 5 µm. 24
Figure 7. SEM image of the µABG from Figure 6. Insets show (left) close up SEM of Al capped W rods in SiO_2 matrix (right) close up SEM of an AlN coupler. 24
Figure 8. Measured transmission for the 9 layer acoustic crystal slab shown in Fig. 1, a SiO_2 reference matrix, and the on wafer electrical feed through of the test set up. A wide (17 MHz) region of ABG induced acoustic attenuation is observed between 59 and 76 MHz. 25
Figure 9. Normalized transmission of the ABG slab in Fig. 1 derived by dividing the transmission of the square lattice ABG by the transmission of the matrix device. The location of the measured bandgap is accurately predicted by FDTD models while the acoustic attenuation of the bandgap is overestimated. 25
Figure 10. W1 (a) and W3 (b) ABG based waveguides realized by removing 1 and 3 rows of W rods from the acoustic crystal in Figure 6. 26
Figure 11. Scanning electron micrograph image of a W2 waveguide realized by removing 2 rows of tungsten scattering inclusions from a square lattice phononic crystal plate. Inset shows close up image of the suspended phononic crystal slab and an AlN transducer. The lattice constant, *a*, is 45 µm and the radius of the W inclusions, *r*, is 14.4 µm. 27
Figure 12. Measured transmission of the W1 ABG waveguide in Figure 10(a), the 9-layer ABG slab in Figure 6 and the matrix material. The W1 waveguide has a single

acoustic propagation band between 62 and 62.5 MHz with a relative transmission of 100% when compared to the matrix device....27
Figure 13. Measured transmission of the W3 ABG waveguide in Figure 10(b), the 9-layer ABG slab in Figure 6 and the matrix material. The W3 waveguide has multiple acoustic propagation bands, nearly reaching a relative transmission of 100% between 69 and 70 MHz....28
Figure 14. Normalized transmission of the W2 waveguide device in figure 7 and of an un-defected, 8-period, square lattice phononic crystal. Several guided modes exist inside the bandgap region including a dominate mode at 68 MHz with a normalized transmission of 1. 28
Figure 15. A) Phononic crystal slab device with chirped AlN piezoelectric couplers. B) Cross-section of an unreleased W/SiO_2 phononic crystal. C) Close-in image of the phononic lattice. The lattice constant is 2.5 µm and the W inclusions are 1.4 µm in diameter. 29
Figure 16. Another image of the phononic crystal device in Figure 15. 30
Figure 17. Measured (blue) and finite difference time domain (green) normalized response of the phononic crystal slab shown in Figure 15. 31
Figure 18. W1 waveguide, formed by removing a single row of inclusions form a phononic crystal, picture and dimensions....31
Figure 19. Measured response of the W1 waveguide in Figure 18. The strongest guided mode is at 781 MHz and has a bandwidth of 2.5 MHz. 32
Figure 20. W3 waveguide, formed by removing three rows of inclusions form the phononic crystal in Figure 16. 32
Figure 21. Measured response of the W3 waveguide in Figure 20. The strongest guided mode is between 1036 and 1055 MHz. 33
Figure 22. (a) Substrate isolation of a thin film resonator using a 1D ¼ wavelength Bragg acoustic mirror stack. While very high reflectivity is obtained for longitudinal waves propagating in the direction of the mirror, the reflection of off axis and shear waves generated by the resonator is degraded, limiting substrate isolation and quality factor. (b) Substrate isolation of a thin film resonator using a 3D phononic crystal. The 3D nature of the crystal reflects incident acoustic waves at any angle and the bandgap covers a wide frequency range to reflect both longitudinal and shear waves....35
Figure 23. Schematic diagram depicting the use of phononic crystal waveguides to allow the acoustic signals from large electro-acoustic transducers to be emitted and detected through small apertures. Decoupling the transducer from the aperture enables higher density acoustic imaging which leads to higher image resolution....36
Figure 24. Schematic diagram containing different types of cavities and filters that can be realized in a 2D defected phononic crystal plate. (a) Point defect series cavity, (b) two point defect series cavities coupled together to form a filter, (c) W1 waveguide with a drop cavity, and (d) two waveguides, one containing a drop cavity, coupled together by a series resonator. Decoupling of the resonant cavity and the electro-acoustic transducer shown in (a) allows the transducer to be realized in high coupling but moderate Q piezoelectric materials while the cavity is realized in high-Q phononic crystal materials. The waveguide filters in (c) and (d) enable distributed acoustic cavities and filters to be realized analogous to microstrip electromagnetic filters commonly used at microwave

frequencies, where an acoustic implementation allows for miniaturization and higher frequency selectivity..38

List of Tables

Table 1. Micro-phononic crystal material combinations and properties. 17

1 INTRODUCTION

Phononic crystals are the acoustic wave equivalent of photonic crystals, where a periodic array of scattering inclusions located in a homogeneous host material causes certain frequencies to be completely reflected by the structure. This creates bandgaps in the frequency response of a phononic crystal. At the micro-scale, phononic crystals are useful for acoustic isolation of vibrating structures such as gyroscopes and mechanical resonators, allowing the rigid attachment of these devices to the substrate. Rigid substrate attachment improves yield, quality factor and immunity to environmental noise sources such as vibration. By strategically placing defects in a phononic crystal, devices such as acoustic waveguides, cavities and filters can be formed. For applications in radio frequency (RF) communications, phononic crystals can realize cavities integrated directly over CMOS circuitry with high frequency selectivity, low insertion loss, and small size, properties not readily achieved together in existing technologies. Defected phononic crystals also offer novel methods for coupling acoustic cavities together to form high order filters that can improve filter performance metrics such as insertion loss and shape factor. Micro-phononic crystal waveguides and focusing devices have the potential to impact acoustic imaging applications such as ultrasound and nondestructive testing by miniaturizing acoustic lenses, performing impedance matching and decoupling the electro-acoustic transducer size and design from the acoustic aperture. The co-location of visible and infrared photonic crystals with phononic crystals operating at commonly used RF communication frequencies becomes possible for micro-scale feature sizes. Designs utilizing these microfabrication techniques enable novel opto-acoustic devices based on phonon-photon interaction such as modulators and optical cooling.

The first complete phononic bandgap was experimentally demonstrated in 1998 [1-3]. Since that time, a great deal of progress has been made in the theoretical analysis and demonstration of phononic crystals [4-11] and phononic crystal based devices such as waveguides [4,12-14], filters [15-18] and structures for acoustic collimation [19], focusing [20], and negative refraction [21,22]. Until recently, the physical realization of phononic crystals has been largely limited to the hand assembling of balls or rods in water, epoxy or air [2-4,9-11,13,15-18,20,22], resulting in large devices that are limited in operating frequencies to below 1 MHz. These hand assembled devices were inherently lossy, time consuming and costly to manufacture, and difficult to reproducibly construct. Recently, utilizing a variety of microfabrication techniques and device topologies, phononic crystals [23-30] and phononic crystal based devices [29] have been realized and experimentally verified at very high frequencies (VHF: 30-300 MHz) and ultra high frequencies (UHF: 300-3000 MHz). A 1D micro-phononic crystal, constructed for surface acoustic waves (SAWs), achieved frequencies approaching 1 GHz utilizing a grating of lines etched in a glass substrate [23]. A subsequent phononic crystal demonstration achieved hypersonic (> 1 GHz) frequencies and 2D operation utilizing interference lithography to place air scattering inclusions in an epoxy host material or matrix [24]. One of the first realizations of 3D micro-phononic crystals was achieved by the self-assembly of polystyrene nanosphere inclusions on a glass substrate subsequently back filled with a silicon oil matrix [25]. Two-dimensional phononic bandgaps were observed for SAWs by etching air hole inclusions, first in a Si matrix [26] and later in a lithium niobate host material [27]. These 2D SAW phononic crystals were co-fabricated with integrated piezoelectric transducers, greatly simplifying micro-phononic crystal characterization when compared to non-integrated approaches such as Brillouin light scattering [24,25] and picosecond transient grating photoacoustic techniques [23]. The integration of piezoelectric couplers with phononic crystals, the realization of micro-phononic crystals in solid materials with low acoustic damping, and the ability to place defects in a phononic crystal though changes in a photolithographic mask, enables the practical application of this technology in areas such as radio frequency (RF) communications and acoustic imaging.

This work focuses on two-dimensional micro-phononic crystals with integrated piezoelectric couplers suspended from the host substrate using Si micromachining techniques. By embedding tungsten (W) scattering inclusions in a suspended SiO_2 matrix [28-31], the 1st VHF and UHF phononic crystal and phononic crystal devices in low loss media are reported. Suspension from the substrate creates Lame` wave phononic bandgap structures and prevents scattering of acoustic energy into the bulk, which is important for realizing devices such as cavities and waveguides in a defected phononic crystal. Coupling between surface and bulk modes has been reported in SAW micro-phononic crystals [23,27] which are rigidly attached to the substrate. The first micro-phononic crystal devices were demonstrated using suspended membrane technology [29] and were later extended to UHF frequencies compatible with mobile communications. In this work acoustic waveguides were realized by omitting rows of W scattering inclusions from a 2D W/SiO_2 phononic bandgap crystal.

2 MICRO-PHONONIC CRYSTAL DESIGN AND ANALYSIS

Phononic crystals can be analyzed in much the same way as semiconductor bandgap materials. In semiconductors electrons are confined to certain energy bands and forbidden from others. The energy spans between accessible bands are referred to as bandgaps. The properties of the bandgap are determined by the size, periodicity and arrangement of atoms in the crystal lattice of the semiconductor which causes diffraction of electrons based on Bloch's theorem. Placing defects in a semiconductor bandgap though doping or application of an electric field allows conduction of electrons in certain energy states within the bandgap.

Similarly for phononic bandgap materials, a periodically spaced array of inclusions forming a crystal lattice can be used to open bandgaps, or frequency ranges where acoustic propagation is forbidden within the crystal. The bandgap center frequency, width (range of frequencies over which phonons can not be transmitted through the material) and depth (the amount of acoustic rejection inside the bandgap frequency region) are determined by the size, periodicity, and arrangement of the inclusions in a background material or matrix and the material properties of the matrix and inclusions. Also analogous to semiconductor bandgap materials, placing defects in a phononic crystal through removal or distortion of the inclusions allows certain frequencies to exist within the bandgap. Phononic bandgap engineering can be used to create cavities, waveguides, focusing and other useful devices inside a phononic crystal. Physically, a phononic bandgap is formed by the diffraction of phonons propagating in a crystal at the interface between the matrix and inclusion materials. The physical origins of phononic bandgaps can be well understood at the micro-scale using classical wave theory to describe the Bragg and Mie resonance based scattering of acoustic waves propagating within the crystal.

A schematic representation of a 2D array of inclusions with acoustic impedance, Z_i, and acoustic velocity V_i, arranged in a square lattice within a host matrix with acoustic impedance, Z_M, and acoustic velocity V_M is shown in figure 1. Also depicted in figure 1 are the distinct ΓX and ΓM directions of acoustic wave propagation inside the crystal. The geometrical parameters, a, which is the lattice constant or pitch of the inclusions, and ,r, which is the radius of each inclusion and together with a defines the volume filling fraction of the inclusions in the matrix, r/a, are also shown in figure 1. Also depicted are the Bragg and Mie resonance conditions essential for opening a wide spectral bandgap utilizing a phononic crystal. The fundamental Bragg resonance frequencies are found where the lattice constants in the ΓX and ΓM directions, a and $\sqrt{2}a$, are equal to one half of the acoustic wavelength [4]. In a square lattice phononic crystal, the fundamental Bragg resonance frequencies in the ΓM and ΓX directions are therefore separated by a factor of $\sqrt{2}$,

$$f(Bragg)_{\Gamma X} = \frac{V_{avg}}{2a} \ , \tag{1}$$

$$f(Bragg)_{\Gamma M} = \frac{V_{avg}}{(2a)\sqrt{2}} , \tag{2}$$

where V_{avg} is the average acoustic velocity in the composite crystal. A good estimate of V_{avg} based on the volume filling fraction of inclusions in a square lattice is given by [32]

$$V_{avg} = \pi\left(\frac{r}{a}\right)^2 V_i + \left(1-\pi\left(\frac{r}{a}\right)^2\right)V_M \ . \tag{3}$$

If the two Bragg resonances are wide enough in frequency to overlap then a phononic bandgap can be realized based solely on the Bragg resonance conditions [4]. The width and depth of each Bragg resonance is dependent on the acoustic impedance mismatch between the matrix and inclusion and maintaining a reasonable volume filling fraction, r/a. The filling fraction must be large enough to restrict transmission through the matrix material around the scattering inclusions. On the other hand, if the filling fraction becomes too high, hopping between the scattering inclusions leads to acoustic transmission. Larger acoustic impedance mismatch between the matrix and the inclusions results in Bragg resonances that are wider in frequency and reflect a greater proportion of the acoustic wave. The acoustic impedance of a material, Z, is

$$Z = \rho V = \sqrt{E\rho} \ , \tag{4}$$

where ρ and E are the density and modulus of the material and the velocity, V, is given by

$$V = \sqrt{\frac{E}{\rho}}. \tag{5}$$

Unlike photonic crystals realized from nonmagnetic materials, where the refractive index (wave impedance) and velocity are linearly related by the constant speed of light in free space, opening a phononic bandgap requires selection of materials with both the proper mass density and modulus to yield the desired acoustic impedance and velocity mismatch between the matrix and inclusions. The amount of acoustic power reflected at the interface between the inclusion and the matrix is

$$\Gamma^2 = \left(\frac{Z_i - Z_M}{Z_i + Z_M}\right)^2. \tag{6}$$

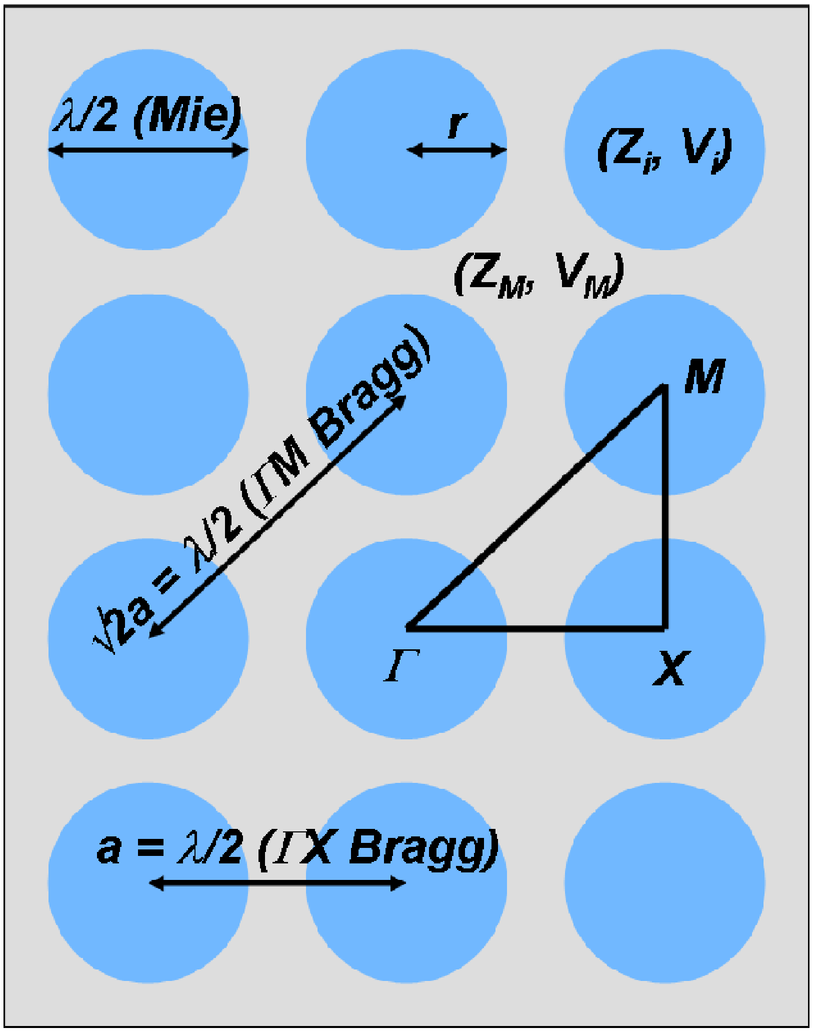

Figure 1. Schematic diagram of a 2D square lattice periodic crystal showing the distinct *ΓX* and *ΓM* directions of acoustic propagation inside the crystal, the lattice pitch, *a*, the lattice filling fraction, *r/a*, and the Bragg and Mie resonance conditions necessary for realizing a spectral bandgap.

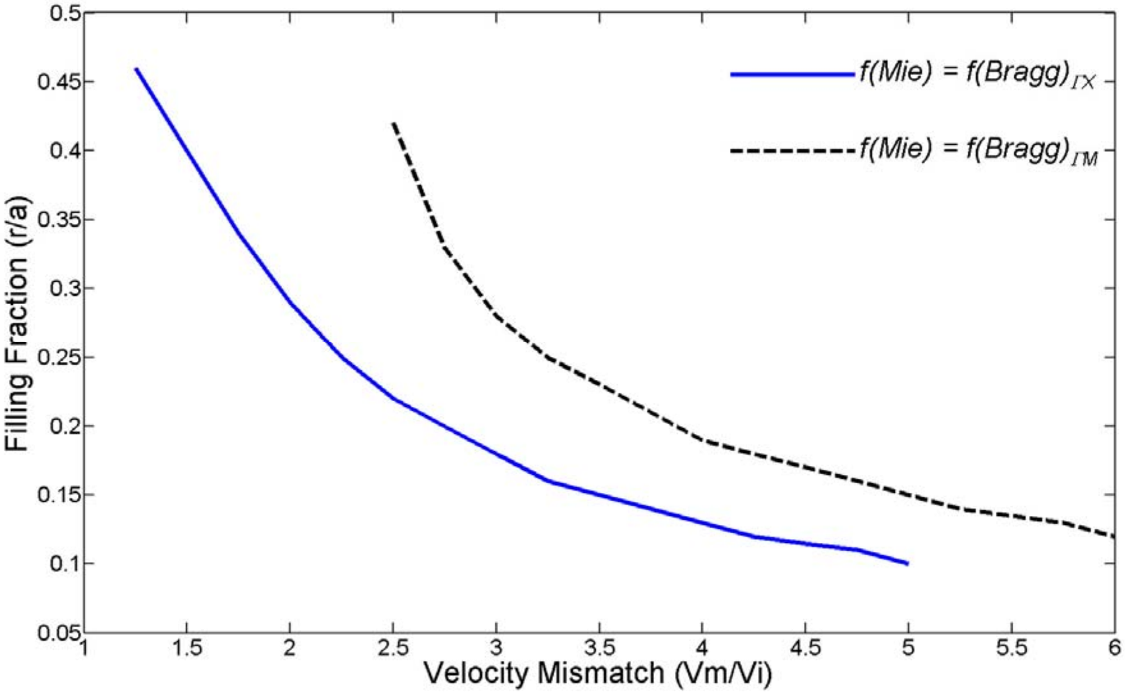

Figure 2. Plot of the phononic crystal filling fraction, *r/a*, that sets the Mie and Bragg resonance conditions shown in figure 1 equal vs. the velocity mismatch between the matrix and scattering inclusion, V_M/V_i. While it is not necessary to set these resonances exactly equal, in order for the Mie resonance to contribute to a phononic bandgap, the width of the Bragg and Mie resonances must overlap which places limits on the desired velocity mismatch between the matrix and inclusion materials in a phononic crystal.

Large acoustic impedance mismatch between the matrix and inclusion is necessary for achieving wide frequency Bragg resonances that overlap to form a phononic bandgap. It is important to note that elastic solids have both a longitudinal and shear velocity for which the Bragg modes must overlap to form a complete phononic bandgap. In a hexagonal lattice the Bragg resonances are separated by √3 which results in a wider gap but requires higher acoustic impedance mismatch to achieve overlap. A similar analysis for hexagonal and honeycomb lattices, presented here for the square lattice only, can be found in [32].

Macro-scale phononic crystals [2-4,9-11,13,15-18,20,22] composed of high velocity balls or rods in a low velocity air, water or epoxy matrix are realized solely from overlapping Bragg resonant scattering. The same is true for micro-scale phononic crystals realized by including low velocity air holes in a high velocity matrix [24,26,27]. As is shown below, overlapping the Bragg and Mie resonance conditions in phononic crystals with very high velocity contrast between the matrix and inclusions is impractical [32].

While it is possible to realize a phononic bandgap based on Bragg diffraction alone [4], an ideal spectral bandgap, observable in all directions, implies strong resonance scattering is needed from each individual unit cell or scattering inclusion [33]. This is accomplished in periodic spectral crystals utilizing the Mie resonance condition shown in figure 1, which ideally is superimposed with the Bragg resonance conditions given in equations 1 and 2 [32] and supplies another resonance for widening the frequency and increasing the acoustic wave reflection of the bandgap. The frequency of the fundamental Mie resonance, which for the circular inclusions in figure 1 is equivalent in all directions, is given by

$$f(Mie) = \frac{V_i}{4r}. \tag{7}$$

From equations 1, 2, 3, and 7 several conclusions can be drawn. First, superimposing or placing the frequency of the Bragg and Mie resonances such that the frequency widths of these resonances overlap requires that the velocity mismatch between the scattering inclusion and matrix material not be too high. Shown in figure 2 is a plot of the filling fraction ratio versus velocity mismatch that sets the fundamental Mie resonance frequency equal to each of the two Bragg resonant frequencies for the square lattice in figure 1. As the velocity mismatch goes to unity, the ratio of *r/a* goes to *0.5*, where the scattering structures touch and the bandgap is compromised. Because the wavelength of the fundamental Mie resonance is necessarily smaller than the fundamental wavelength of both the *ΓX* and *ΓM* Bragg resonances, the Mie and Bragg resonances can not be set equal for the case where the acoustic velocity in the scattering inclusion is greater than that in the matrix. While setting the Bragg and Mie resonance frequencies equal represents an extreme case, it is required that the finite frequency range of the Mie and Bragg resonances overlap for the Mie resonance to contribute to the gap. At the micro-scale, previously reported measured bandgaps have gap-to-mid-gap ratios less than 25% [25-30]. Thus, figure 2 shows the general trend of required filling fraction versus velocity mismatch. Since the majority of macro-scale phononic bandgap crystals found in the literature [2-4,9-11,13,15-18,20,22] are constructed of high velocity scattering inclusions in a low velocity matrix where, $V_i >> V_M$, it can be determined that these reported bandgaps are formed by wide overlapping Bragg resonances without the presence of Mie resonant scattering. While it would be possible to overlap overtones of the two Bragg modes with the fundamental Mie frequency in this case, the frequencies of the reported phononic bandgaps correspond well with the fundamental Bragg frequencies given in equations 1 and 2. In the opposite case, as the velocity of the matrix becomes much greater than that in the scatterer, the optimum ratio of *r/a* that overlaps the Bragg and Mie resonances tends to *0* and the amount of Bragg scattering dramatically decreases as the waves are free to propagate around the scatterers. This case, $V_M >> V_i$, is seen in micro-phononic crystals realized by including air scattering inclusions in a solid matrix [24,26-27]. As was the case in the other extreme example, $V_i >> V_M$, very high acoustic impedance mismatch leads to strong overlapping Bragg resonances given the proper filling fraction is chosen. It is also possible in this case to overlap high order Mie resonances with the Bragg diffraction and increase the frequency width of the gap, although the relative frequency width of such high order resonances is much less than that of fundamental modes. Thus, phononic crystals realized by placing air inclusions in an elastic solid are formed purely by overlapping Bragg resonances. Nearly all reported theoretical and physical designs of phononic crystals formed by air inclusions in a solid matrix require large filling fractions to open a complete bandgap [8,12,26,27,33], resulting in features that are difficult to fabricate repeatedly, especially at high frequencies [34].

3 MICRO-PHONONIC CRYSTAL MATERIAL CONSIDERATIONS

From the results presented above several conclusions can be drawn. First, it is possible to realize phononic bandgap crystals at the micro-scale in both cermet [28-30], defined as high acoustic impedance inclusions in a low acoustic impedance matrix, and network [26,27], defined as low acoustic impedance inclusions in a high acoustic impedance background matrix, topologies. Table 1 summarizes the parameters for several promising phononic crystal material sets readily available at the micro-scale.

Table 1. Micro-phononic crystal material combinations and properties.

Matrix	Inclusion	Topology	Reflection Coefficient (Γ^2)	Velocity Mismatch (V_m/V_i)
Elastic Solid	air	Network	~1	> 10
SiO_2	W	Cermet	0.58	1.3
SiO_2	Pt	Cermet	0.42	2.1
SiO_2	Mo	Cermet	0.41	1.0
Poly-Si	W	Cermet	0.4	1.9
Poly-Si	Pt	Cermet	0.25	3.0
Poly-Diamond	SiO_2	Network	0.45	3.2

3.1 Air/solid phononic crystals

Air hole inclusions placed in nearly any solid material with low acoustic damping can be used to realize network topology phononic crystals. Air inclusions reflect, Γ^2, nearly 100% of the acoustic power at the matrix-inclusion interface. Provided the correct filling fraction is used, the large Γ^2 results in wide, overlapping Bragg resonances and achieves a phononic bandgap. The required filling fractions to achieve wide bandgap air/solid phononic crystals are typically large [27,34], $r/a > 0.4$, resulting in small line features between the inclusions. The ability to pattern these fine features limits the maximum frequency of operation to well below that of solid/solid phononic crystals. Because the speed of sound in air is much less than the acoustic velocity in any low-loss solid, it is not possible to overlap the fundamental Mie resonance with the fundamental Bragg resonances. Higher order Mie resonances may contribute to the fundamental gap, but these resonances are not wide due to their high order nature. This limits the gap width for a given phononic crystal lattice configuration. Recent results obtained for a micro-phononic crystal formed by placing a honeycomb lattice of air holes in a suspended Si plate [35] demonstrates measured bandgap widths comparable to those seen in solid/solid square lattice micro-phononic crystals [28-30]. The honeycomb lattice, when compared to hexagonal and square lattices, has also been shown to provide wider bandgaps for a given matrix/inclusion material set in photonic [36] and macro-scale phononic crystals [10].

3.2 Solid/solid phononic crystals

To open a wide spectral bandgap utilizing solid inclusions in a solid matrix to form a phononic crystal at the micro-scale requires careful selection of the materials. Both materials should have low acoustic damping to allow the realization of high-Q cavities and low-loss waveguides. If possible, the materials should be commonly used in integrated circuit or microsystem fabrication such that the processes and tools for depositing, etching and micromachining these materials are well developed. The acoustic velocity in the materials should be as high as possible, while still observing the proper velocity mismatch, to achieve the highest possible frequency limited by minimum fabrication tolerances. In all solid/solid phononic crystals, the acoustic impedance mismatch between the matrix and inclusions should be maximized and, ideally, the acoustic velocity in the inclusion should be less than that in the matrix with the proper velocity mismatch from figure 2 to allow superposition of the Mie and Bragg resonance conditions. Since maximum acoustic impedance mismatch is desired and the ideal velocity mismatch is bounded, from equation 4, large mass density mismatch between the matrix and inclusion materials is required to form the widest possible phononic bandgaps.

Of materials commonly processed at the micro-scale, W has the highest acoustic impedance, 89 MΩ, owing to its very high mass density, 19,000 kg/m^3, and moderately high acoustic velocity, 4.6 km/s. Since high velocity materials are desired to achieve high frequency operation, W is best utilized as the inclusion material in a cermet topology phononic crystal. Other commonly microfabricated materials that are suitable to use as inclusions in a cermet topology phononic crystal are platinum, Pt, and Molybdenum, Mo. These materials have 33% lower acoustic impedance resulting in bandgaps that are less wide and deep.

Of low loss, high velocity materials commonly available in microfabrication facilities, SiO_2 has the lowest acoustic impedance, 13 MΩ, making it an ideal candidate for use as the matrix material in cermet topology micro-phononic crystals. When combined with W inclusions, a large reflection coefficient, Γ^2, of 58% is obtained. The optimum filling fraction, r/a, for achieving wide bandgap square lattice W/SiO_2 phononic crystals is 0.32 [30], greatly relaxing the fabrication tolerances when compared to air/solid crystals [27,34]. In [30] the optimum ratio for maximizing the gap depth of a W/SiO_2 phononic crystal was found using FDTD modeling to be 0.44, precisely predicted from the direct overlap of the ΓX Bragg and Mie resonance conditions in figure 2 for a velocity mismatch of 1.3. Single crystal or polycrystalline silicon are also good choices for the matrix material. When paired with W inclusions the reflection coefficient for a Si matrix is reduced by 31% when compared to a SiO_2 matrix. The mechanical quality factor, Q, and the acoustic velocity, however, are both higher in Si than in SiO_2. The slightly higher velocity mismatch between Si and W gives an optimum volume filling fraction, r/a, for maximizing the gap width of 0.26, very close to the optimum value of 0.25 for minimizing the lithography requirements at a given frequency. Combined with the overall higher sound velocity, W/Si phononic crystals may be the best candidates for scaling to frequencies well in excess of 1 GHz. If a network topology is desired, polycrystalline diamond is an excellent choice for the matrix material due to its high acoustic impedance and very high acoustic velocity. As shown in Table 1, if a low acoustic impedance inclusion such as SiO_2 is used, network topology solid/solid micro-phononic crystals can obtain similar reflection coefficients and velocity mismatch as their cermet counterparts.

4 MICRO-SCALE PHONONIC CRYSTAL MODELING

Modeling was performed using Finite Difference Time Domain (FDTD) method. Compared to other methods, FDTD has the unique advantage of being able to assess PnC gap depths and slab mode energies in finite-thickness slabs. FDTD is based on explicit integration of elastic propagation equations on a discrete 3-D cubic grid. A longitudinal displacement wave with Gaussian profile is launched in the in-plane *z*-axis, which is terminated by Mur absorbing boundary conditions in both directions. Data is collected on the opposite side of the discretized PnC model and Fourier transformed to obtain frequency dependent transmittance, normalized to the response of the matrix material provided by a second simulation. An illustration of these arrangements is provided in Figure 3. Details of FDTD method can be found elsewhere [5].

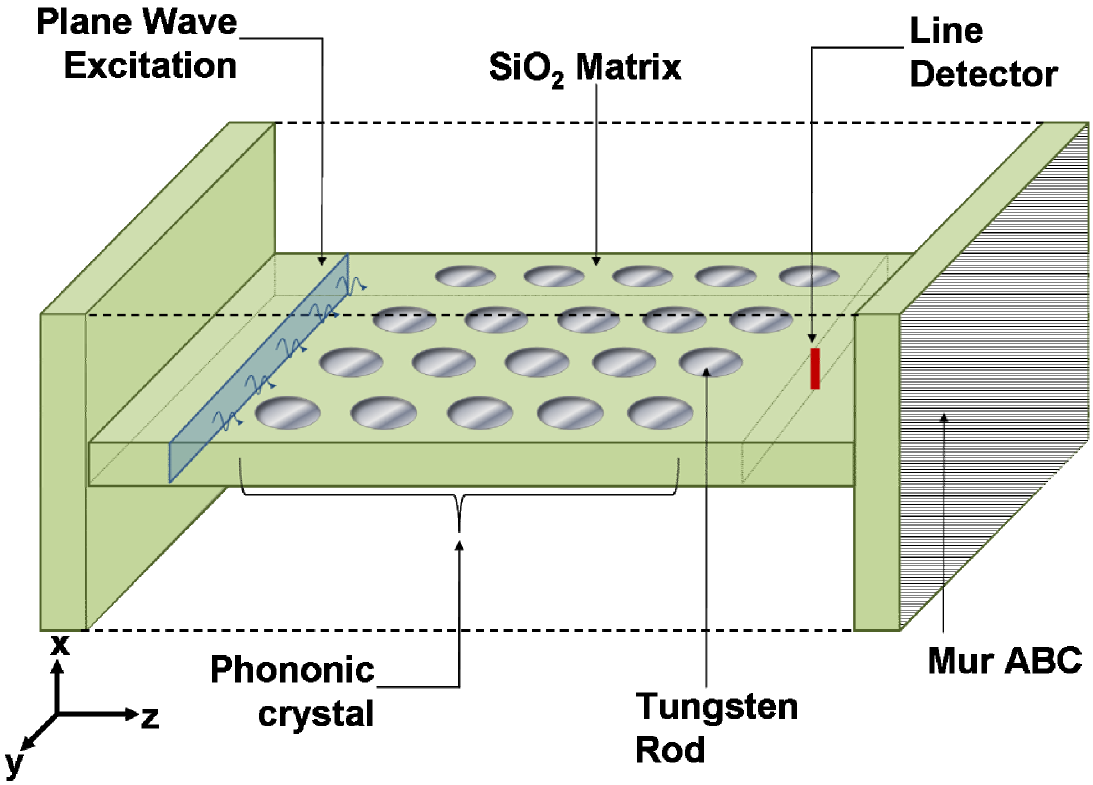

Figure 3. A representation of FDTD simulations of phononic crystals with finite thickness. PnC slab is surrounded with air buffers terminated by periodic boundary conditions in the x-axis, periodic boundary conditions terminating the phononic crystal in the y-axis and matrix material (SiO_2) covered Mur absorbers in the z-axis.

Axes in the transverse direction are terminated with periodic boundary conditions. Periodic boundaries can be used in modeling of infinitely thick PnC's in bulk acoustic wave (BAW) mode. When studying megahertz or below PnC's fabricated in ultrathin slabs as compared to the lattice constant, an infinitely thick PnC FDTD model has proved to be sufficient as the slab resonances of such devices lay well above the bandgap, while the infiniteness of the thickness of the numerical model would push such resonances to identically zero frequencies. For micro-scale phononic crystals however, these modes reside in the gap during gigahertz operation, requiring modeling of a finite thickness PnC slab surrounded by air. Air modeling deserves special consideration because i) numerical instability is introduced by its very low density, ii) there are difficulties using Mur absorbers at air boundaries due to air behaving as a liquid with zero shear and low longitudinal wave velocities. In particular, Mur absorbers cannot be utilized at a liquid boundary since their formulation assumes nonzero wave velocities. We model air at a slightly higher density of 0.1 kg/m^3 to mitigate the former issue without impact on modeling because the impedance contrasts (and thus reflectance) between air and other materials remain very high even after the modification. The latter issue is overcome by i) surrounding the slab with a sufficiently thick (at least three times the lattice periodicity, a) air buffer, ii) using periodic boundaries in transverse directions (as the fabricated samples are extremely wide in that dimension), and iii) placing a very thin layer of matrix material to cover Mur absorbers in the longitudinal directions (along z-axis). While periodic boundary usage per (ii) is expected to give an effect of periodically repeating PnC slabs separated by air buffers, our tests indicate energy transmission (thus cross-talk between adjacent slabs) via air remains negligible so long as the air buffer is sufficiently thick.

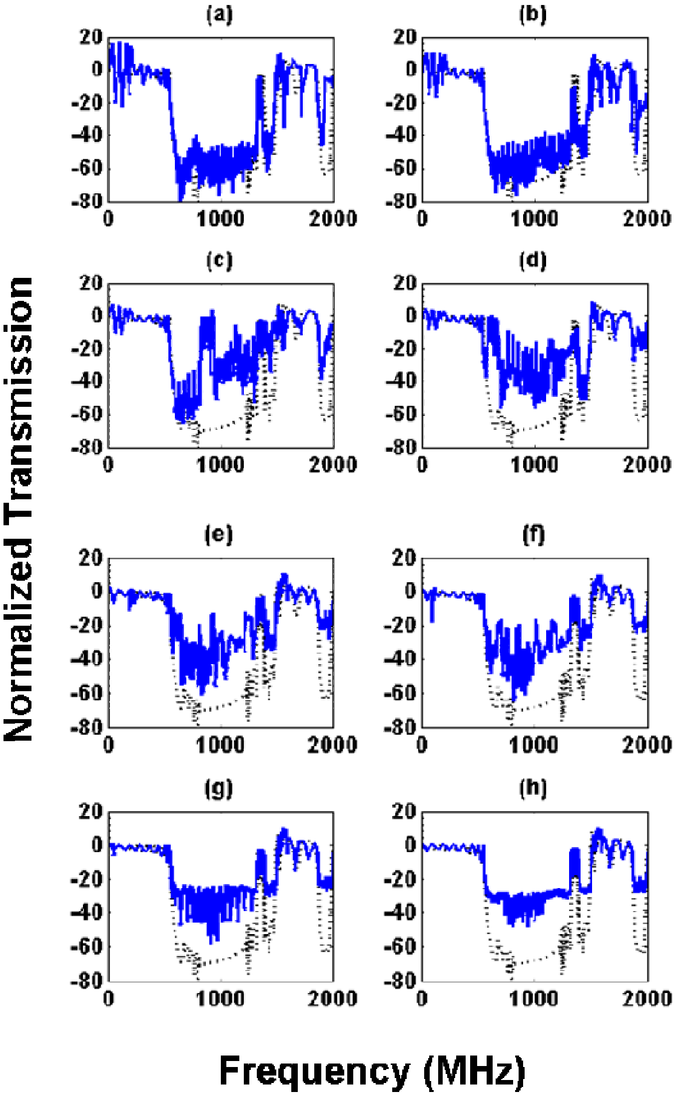

Figure 4. Normalized transmission (dB) vs. frequency (MHz) results for finite-thickness slabs with thicknesses (a) 0.25*a* (b) 0.5*a* (c) *a* (d) 1.5*a* (e) 5*a* (f) 10*a* (g) 25*a* (h) 50*a* where *a* is the lattice periodicity. Blue continuous lines belong to finite-thickness slabs; black dotted lines are infinite-thickness structure result for reference.

A theoretical study of thickness effects was made in order to guide the experimental efforts. Normalized transmission vs. frequency results for various slab thicknesses (blue continuous lines) compared to an infinite thickness structure (black dotted lines) are shown in Figure 4. We conventionally define the minimum acceptable gap depth to be -20 dB of rejection. Our results indicate that for a lattice of periodicity *a*, only ultra thin (thickness < *a*) or ultra thick slabs (thickness ≥10*a*) show gaps untainted by slab modes. It is understood that very thin slabs support very few slab modes, whereas very thick slabs support very high number of modes with low average energy. This abundance of modes is visible as a raised baseline for the thickest slabs shown in Figure 2. In contrast, gap depths for ultra-thin slabs almost match the gap depth for the infinitely thick reference case. Some slab mode resonances can be noticed immediately. For instance, for a slab thickness *a*, the resonance frequency observed in Figure 2 matches the well-known resonance formula $d=n\lambda/2$ for the slab thickness, immediately indicating a transverse mode. For other thicknesses, anticipation is less trivial as resonances for transverse, shear and flexural modes might be present. It is also possible to have windows of opportunity devoid of resonances for arbitrary thicknesses; however these form the exception rather than the rule and given tolerances in manufacturing processes besides other factors, are best avoided.

5 MICRO-SCALE PHONONIC CRYSTAL FABRICATION

5.1 VHF Phononic Crystal Fabrication

The μABG fabrication process shown in Fig. 5 begins (a) with a 0.6 μm SiO_2 deposition and deposition of a 2 μm undoped polySi release layer. Next, a 0.4 μm Al bottom interconnect layer is sputter deposited and patterned. This Al also serves to protect the bottom of the W inclusions during release. The ABG matrix is formed through the plasma enhanced tetraethylorthosilcate (PETEOS) deposition of 4 μm of SiO_2 which is subsequently polished to remove the topography created by the Al. (b) Trenches in the oxide are etched followed by the conformal chemical vapor deposition (CVD) of 1.2 μm of W which forms contacts to the bottom electrode of the AlN couplers and part of the high density W inclusions. The W layer is polished until it remains only where the trenches were etched in the oxide leaving concentric W rings. The total amount of W than can be deposited prior to this polishing step is limited by stress in the CVD W film to 1.2 μm, requiring a 2-step process to form the W ABG inclusions. (c) The formation of the W scatterers is completed by filling in the rings using an additional oxide etch, W deposition, and polish. Next a Ti/TiN/Al bottom electrode is deposited followed by the sputter deposition of 0.75 μm of AlN. The AlN film is highly c-axis oriented with an x-ray diffraction rocking curve full width half maximum of 1.5° which results in strong electro-acoustic coupling. The AlN is patterned and a 0.4 μm Al top electrode is deposited. This Al layer protects the top of the W acoustic reflectors during the release. (d) Finally, holes are etched through the oxide down to the polySi release layer and the devices are released in dry SF_6. Using a thin polySi release layer, as opposed to the Si substrate, prevents etch loading during release and allows large structures to be released through small holes. The process is 7 levels and is post-CMOS compatible provided the Si release layer is deposited at low temperature.

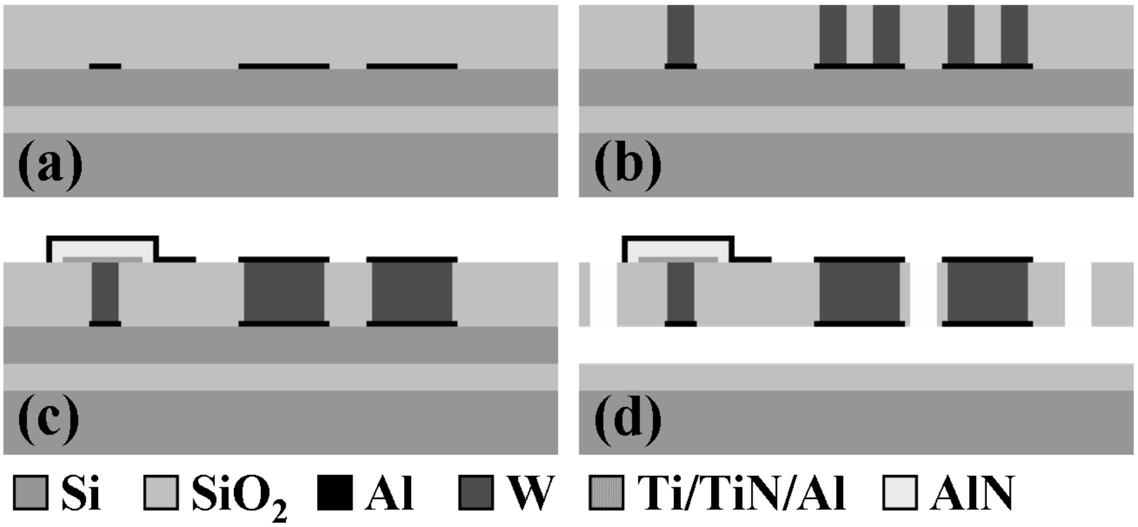

Figure 5. Micro-ABG process flow.

5.2 UHF Phononic Crystal Fabrication

Fabrication of ultra high frequency (UHF) phononic crystals at frequencies approaching 1 GHz is identical to that of the VHF crystals shown in Figure 5 with two exceptions. First, the thickness of the SiO_2 deposition and thus the thickness of the phononic crystal slab is not 4 μm, but instead is taken from Figure 4 based on the lattice constant. Second, at frequencies approaching 1 GHz, and entire W inclusion can be filled in a single W deposition eliminating the need for step (b) in Figure 5.

6 PHONONIC CRYSTAL DEVICE OPERATION AND MEASURED PERFORMANCE

6.1 VHF Phononic Crystal Devices

A 67 MHz microfabricated W/SiO_2 square lattice phononic crystal plate is pictured in Figure 6. Acoustic energy is coupled into and out of the device in the form of acoustic waves using electrically driven AlN piezoelectric couplers. The couplers are tapered on the end to provide a wide drive and sense bandwidth necessary for characterizing the phononic crystal. Acoustic frequencies inside the gap cannot propagate between the two AlN couplers which is measured as a drop in transmission (S21) when compared to a reference matrix device, which has identical dimensions, couplers, and release holes but no W inclusions to form a phononic band-gap. An SEM image of the microfabricated 67 MHz phononic crystal plate is shown in Figure 7. The lattice constant, *a*, is 45 μm and the radius of the W inclusions, *r*, is 14.4 μm, yielding a volume filling fraction, *r/a*, of 0.32. The release holes in the center of the W inclusions have a radius of 5 μm and the phononic crystal plate is 3.6 μm thick.

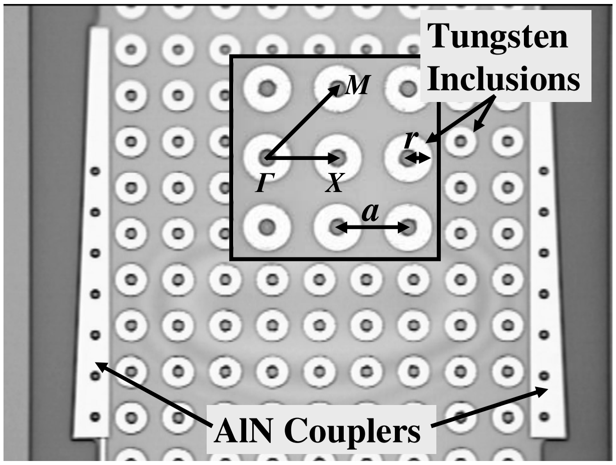

Figure 6. Micro-ABG slab with integrated AlN electro-acoustic couplers. The ABG is realized by including W scatterers in an oxide matrix. Acoustic frequencies within the gap can not pass between the AlN couplers. Inset shows close up image of the W scatterers and release holes. The lattice constant, *a*, is 45µm and *r* is 14.4 µm, yielding a volume filling fraction of 0.32. The release holes in the center of the W inclusions have a radius of 5 µm.

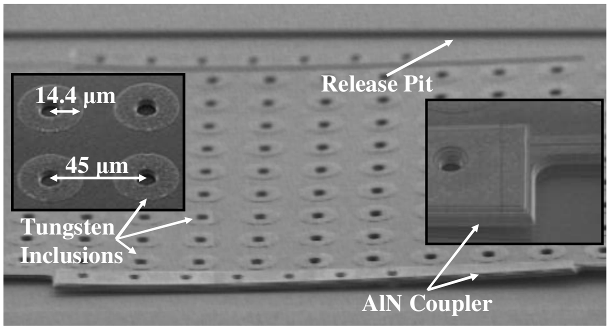

Figure 7. SEM image of the µABG from Figure 6. Insets show (left) close up SEM of Al capped W rods in SiO_2 matrix (right) close up SEM of an AlN coupler.

The measured transmission (S21) of the 67 MHz phononic crystal device pictured in Figure 6 and of the SiO_2 reference matrix are shown in Figure 8. All phononic crystal experiments were performed on a probe station in air using a network analyzer, where the output of the network analyzer was used to launch an acoustic wave into the device via an AlN electro-acoustic coupler. On the opposite side of the device, acoustic waves are detected using the other AlN coupler and fed into the sense input of the network analyzer. Figure 9 shows the normalized transmission for the micro-phononic crystal device in Figure 6, which is derived by dividing the transmission through the phononic crystal structure by the transmission through the reference matrix. The data shows a phononic band-gap between 59 MHz and 76 MHz including an area from 63 MHz to 72 MHz where transmission is attenuated by > 25 dB. The measured gap has a center frequency of 67.5 MHz and a width of 17 MHz or $(\Delta w/w_g) = 25\%$. The predicted band-gap [30] using FDTD modeling from 53 MHz to 80 MHz closely matches the measured band-gap in Fig. 4. As presented in [30], the holes in the center of the W inclusions required to release the relatively large structures at VHF frequencies from the substrate serve to narrow the band-gap. This problem is alleviated for micro-phononic crystals at GHz frequencies where the devices are small enough to completely undercut from the periphery, eliminating problematic release holes from the crystal structure.

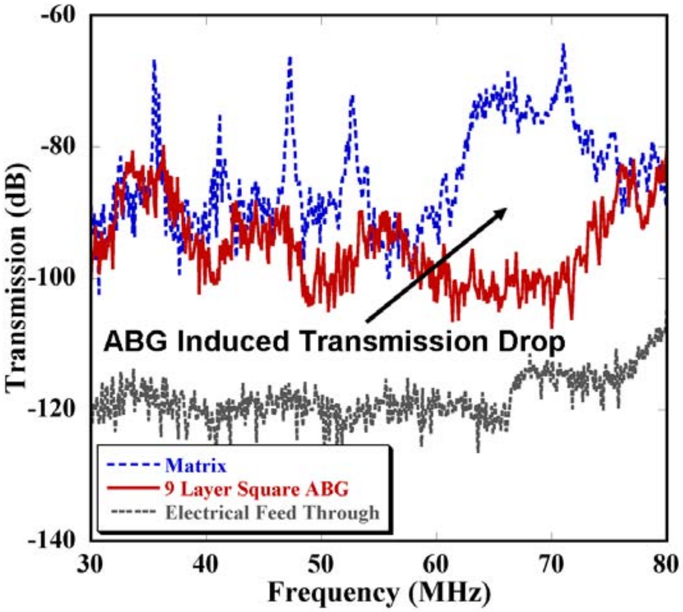

Figure 8. Measured transmission for the 9 layer acoustic crystal slab shown in Fig. 1, a SiO_2 reference matrix, and the on wafer electrical feed through of the test set up. A wide (17 MHz) region of ABG induced acoustic attenuation is observed between 59 and 76 MHz.

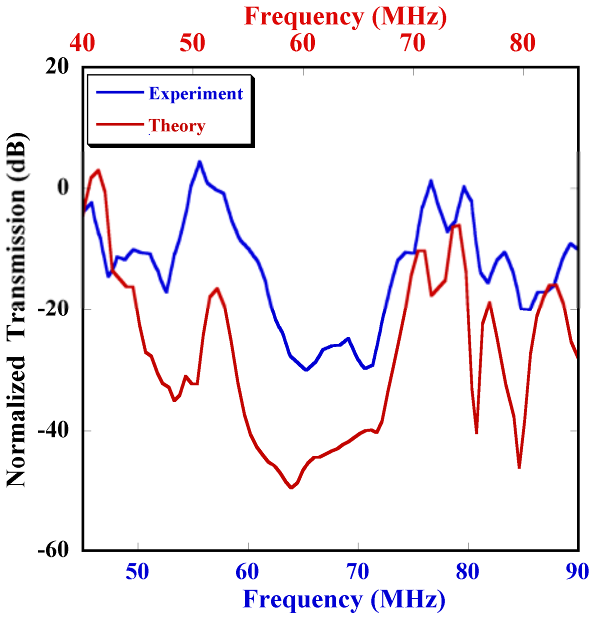

Figure 9. Normalized transmission of the ABG slab in Fig. 1 derived by dividing the transmission of the square lattice ABG by the transmission of the matrix device. The location of the measured bandgap is accurately predicted by FDTD models while the acoustic attenuation of the bandgap is overestimated.

Both W1, W2 and W3 waveguides, pictured in Figure 10 and Figure 11, have been designed by removing 1, 2 and 3 rows of W inclusions between the AlN couplers in the 67 MHz acoustic crystal shown in Figure 6. The W1 and W3 waveguides in Figure 10 have been characterized with the results shown in Figure 12 and Figure 13. Also included in Figure 12 and Figure 13 for reference are the response of the 9-layer square lattice ABG slab in Figure 6 and a matrix device measured on the same wafer as the guide. The W1 waveguide propagates a single waveguiding band between 62 and 62.5 MHz with 100% relative transmission when compared to the matrix device. This indicates that waveguiding via a defected μABG does not introduce loss in addition to that of the couplers and the matrix material itself. The W3 waveguide propagates modes in multiple bands achieving nearly 100% relative transmission between 69 and 70 MHz. The measured normalized transmission of the suspended membrane W2 waveguide and of an undefected, 8-period square lattice phononic crystal is presented in Figure 14. Several modes where acoustic transmission is permitted though the defected bandgap crystal are seen in Figure 14, with a dominant mode at 68 MHz where the relative transmission is equal to 1, indicating no additional loss is created by the W2 waveguiding.

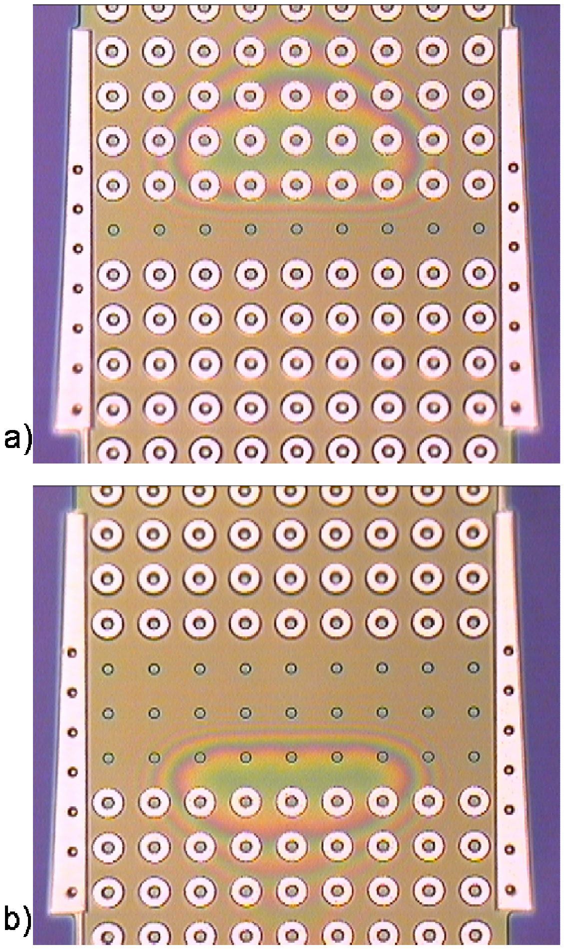

Figure 10. W1 (a) and W3 (b) ABG based waveguides realized by removing 1 and 3 rows of W rods from the acoustic crystal in Figure 6.

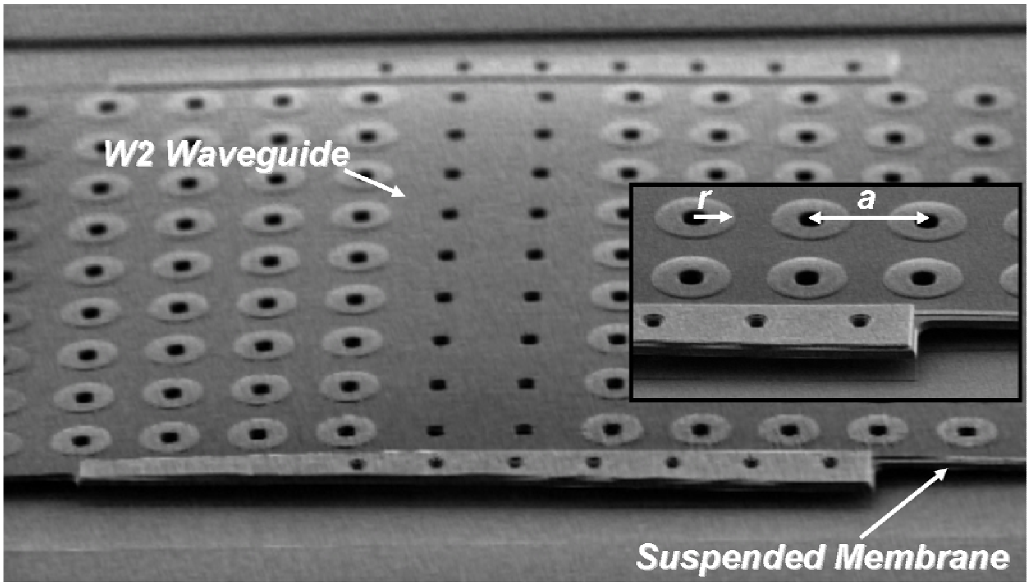

Figure 11. Scanning electron micrograph image of a W2 waveguide realized by removing 2 rows of tungsten scattering inclusions from a square lattice phononic crystal plate. Inset shows close up image of the suspended phononic crystal slab and an AlN transducer. The lattice constant, *a*, is 45 μm and the radius of the W inclusions, *r*, is 14.4 μm.

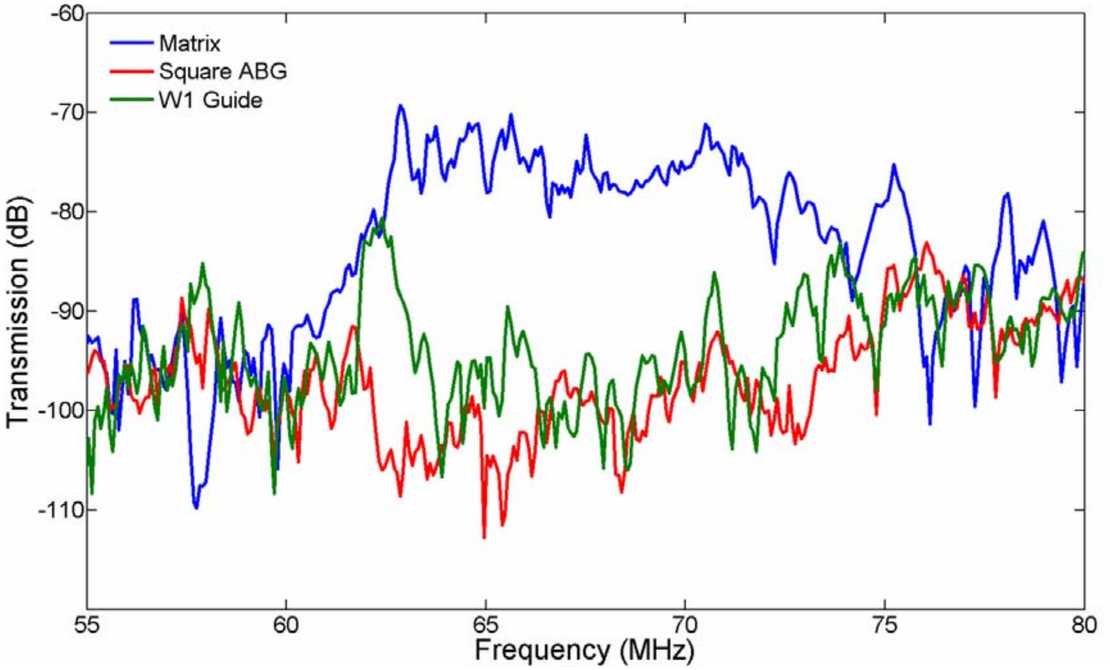

Figure 12. Measured transmission of the W1 ABG waveguide in Figure 10(a), the 9-layer ABG slab in Figure 6 and the matrix material. The W1 waveguide has a single acoustic propagation band between 62 and 62.5 MHz with a relative transmission of 100% when compared to the matrix device.

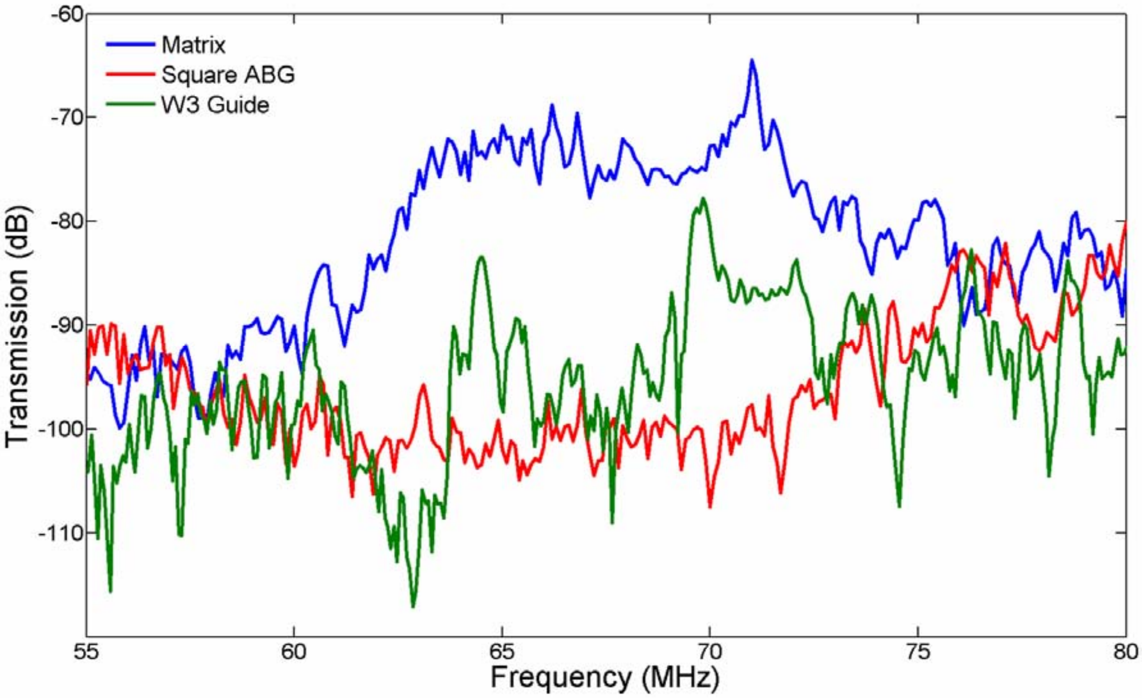

Figure 13. Measured transmission of the W3 ABG waveguide in Figure 10(b), the 9-layer ABG slab in Figure 6 and the matrix material. The W3 waveguide has multiple acoustic propagation bands, nearly reaching a relative transmission of 100% between 69 and 70 MHz.

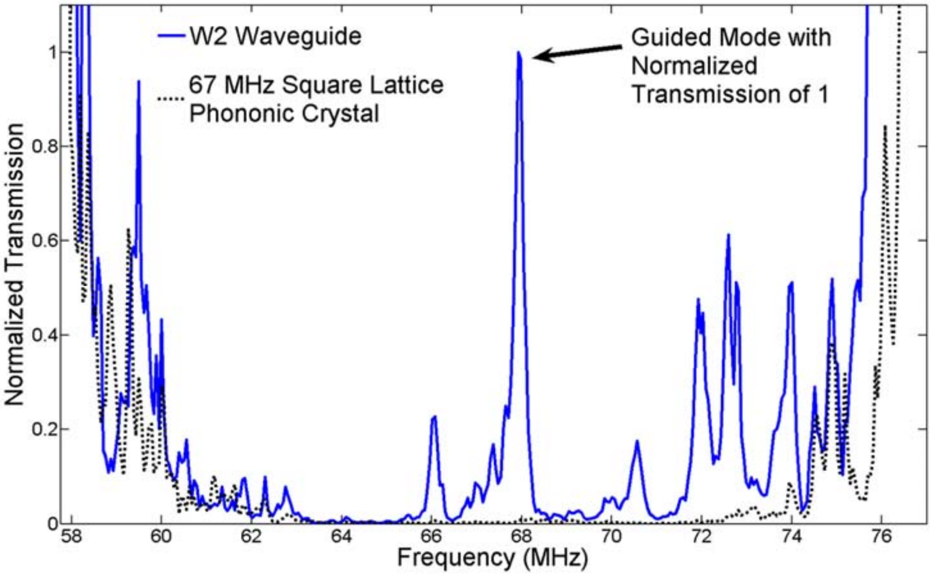

Figure 14. Normalized transmission of the W2 waveguide device in figure 7 and of an un-defected, 8-period, square lattice phononic crystal. Several guided modes exist inside the bandgap region including a dominate mode at 68 MHz with a normalized transmission of 1.

6.2 UHF Phononic Crystal Devices

Shown in Figure 15 are scanning electron microscope (SEM) images of an ultra high frequency (UHF) W/SiO_2 phononic crystal slab fabricated using the process reported in above. Figure 15 A) shows an image of the full phononic crystal slab device including the chirped AlN piezoelectric couplers. Careful inspection reveals that the pitch and width of the top metal electrodes on the AlN couplers varies across the device. This widens the coupler bandwidth and allows the entire frequency span of the phononic crystal to be characterized using 14 couplers designed for slightly different frequency spans similar to the technique reported in [35]. Figure 15 B) shows a cross-section of an unreleased phononic crystal slab while Figure 15 C) shows a zoomed in profile image of a released phononic crystal. The poly-Si release layer is clearly visible under the W/SiO_2 phononic crystal in Figure 15 B). The phononic crystal is 18 periods long (between couplers) and is 42 period wide. The W inclusions are 1.4 µm in diameter, *d*, and are arranged in a square lattice with a lattice constant, *a*, of 2.5 µm, yielding a filling fraction, *d/2a*, of 0.28. One key advantage of forming the phononic crystal from two solid materials with similar sound velocities is that deep (rejection), wide (frequency span) phononic bandgaps can be formed for filling fractions near 0.25 [37]. A filling fraction, *d/2a*, of 0.25 results in the size of the inclusion being equal to the minimum spacing between inclusions. This minimizes as much as possible the lithography requirements for a given lattice constant and bandgap frequency. Another advantage of solid/solid phononic crystals is that the bandgap width and depth is insensitive to filling fraction variation for filling fractions near the optimum *d/2a* that maximizes the bandgap width. The result is that lithographic and etching fabrication process biases that systematically vary the inclusion diameter and filling fraction do not adversely impact performance. An additional image of this UHF phononic crystal is shown in Figure 16.

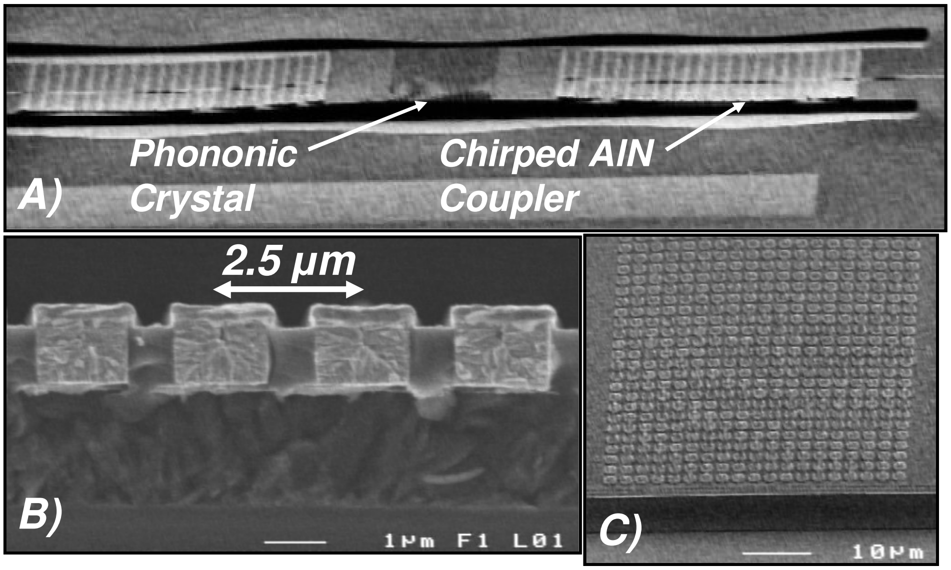

Figure 15. A) Phononic crystal slab device with chirped AlN piezoelectric couplers. B) Cross-section of an unreleased W/SiO_2 phononic crystal. C) Close-in image of the phononic lattice. The lattice constant is 2.5 µm and the W inclusions are 1.4 µm in diameter.

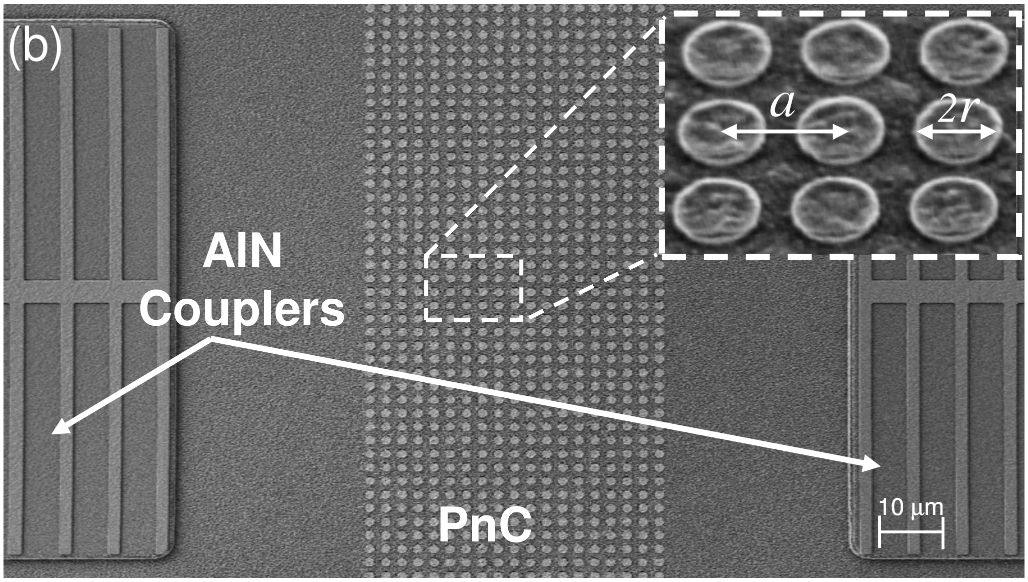

Figure 16. Another image of the phononic crystal device in Figure 15.

To characterize the UHF phononic crystal, 14 chirped AlN couplers were designed to continuously cover the 700 MHz to 2 GHz frequency range. Each of these couplers was connected to a phononic crystal slab as shown in Figure 16 and to a suspended SiO_2 membrane that is identical to the slab in Figure 16 except that no phononic crystal is included between the couplers. This device, containing just a SiO_2 membrane between two chirped AlN couplers is hereafter referred to as the matrix. The transmission between the couplers was measured for the 14 matrix/coupler pairs and a composite matrix response was formed as described in [37]. The transmission was then measured between the 14 phononic crystal/coupler pairs and was normalized to the matrix by dividing the phononic crystal response by the matrix response to remove the effect of the couplers [37]. The normalized phononic crystal response is shown in Figure 17 along with the response predicted by finite difference time domain (FDTD) modeling that includes the slab thickness which in this case was 1.85 µm or 0.74a. The measured bandgap is centered at 943 MHz and has a maximum depth of 35 dB. The bandgap width is 417 MHz or 44% of the bandgap center frequency. Utilizing solid/solid phononic crystals and eliminating the release holes required at VHF frequencies results in a bandgap width-to-center-frequency percentage twice that previously reported for microscale phononic crystal slabs [26-30]. As can be seen in Figure 17, the phononic bandgap is well predicted by the FDTD model except for the region between 600 and 700 MHz where the measured bandgap closes but the FDTD bandgap remains open. This is mainly due to poor coupler response between 600 and 700 MHz. The high frequency end of the bandgap is accurately modeled by FDTD as is much of the acoustic structure in this region.

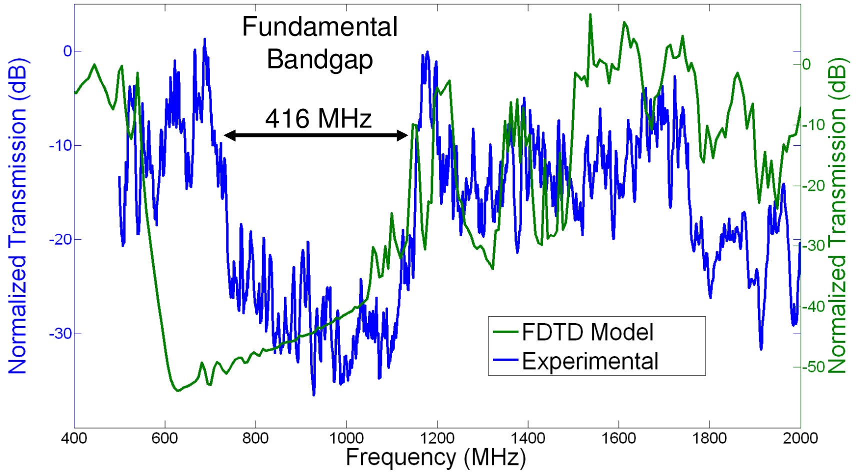

Figure 17. Measured (blue) and finite difference time domain (green) normalized response of the phononic crystal slab shown in Figure 15.

An optical image of a W1 waveguide, formed by removing 1 row W inclusions from the phononic crystal in Figure 16, is shown in Figure 18. The response of the W1 waveguide, measured using the normalization technique described above is shown in Figure 19. The primary propagating mode is centered at 781 MHz and has a bandwidth of 2.5 MHz. The normalized insertion loss of the propagating mode is 0.1 or 10 dB. There are several other modes all with higher loss that are also seen to propagate within bandgap region.

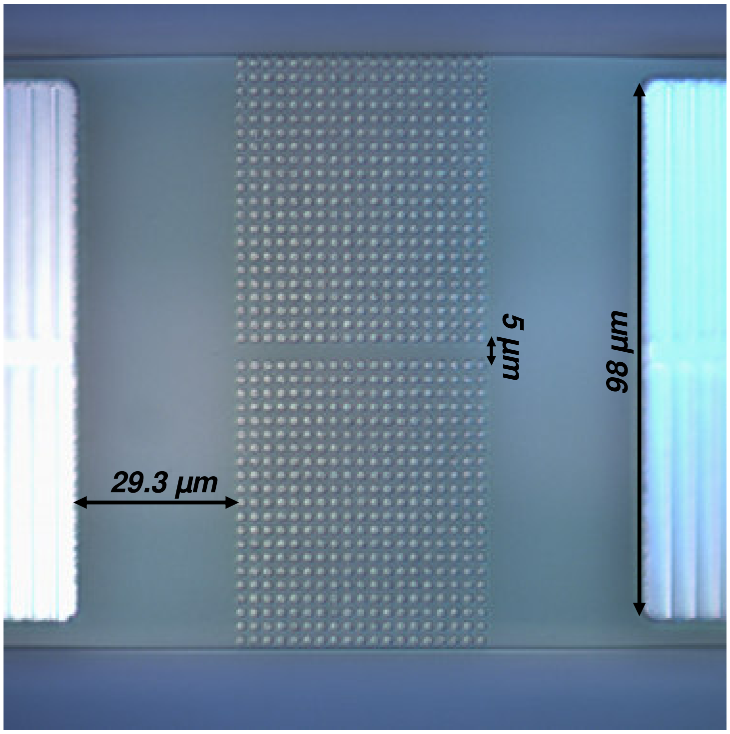

Figure 18. W1 waveguide, formed by removing a single row of inclusions form a phononic crystal, picture and dimensions.

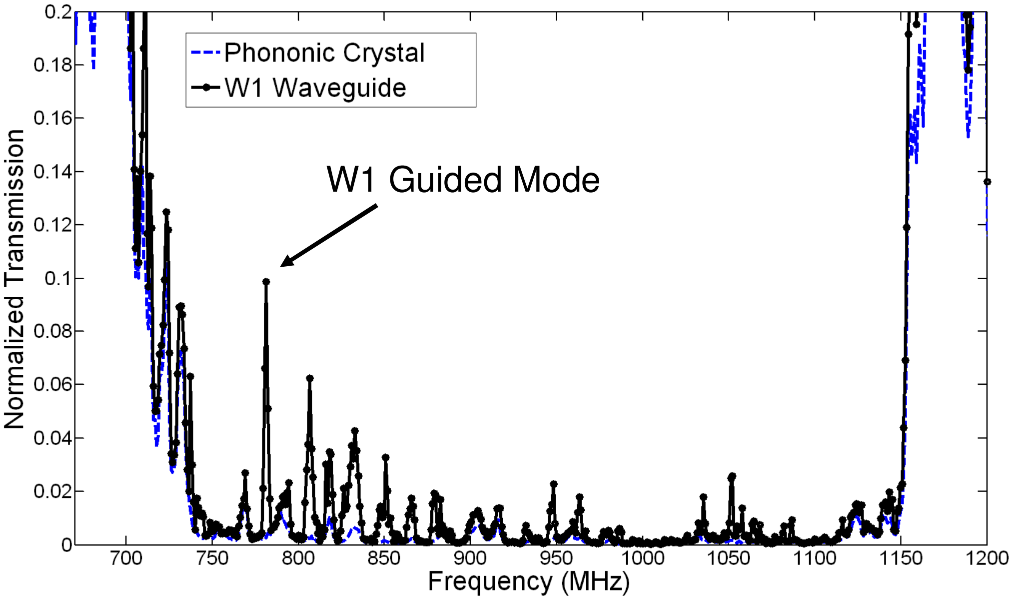

Figure 19. Measured response of the W1 waveguide in Figure 18. The strongest guided mode is at 781 MHz and has a bandwidth of 2.5 MHz.

An optical image of a W3 waveguide, formed by removing 3 rows of W inclusions from the phononic crystal in Figure 16, is shown in Figure 20. The propagating mode is between 1036 and 1055 MHz and has a minimum insertion loss of 14 dB. As expected, the bandwidth of the W3 waveguide is wider than that of the W1 waveguide. No additional modes are observed within the bandgap region for the W3 waveguide outside the immediate vicinity of the primary mode.

Figure 20. W3 waveguide, formed by removing three rows of inclusions form the phononic crystal in Figure 16.

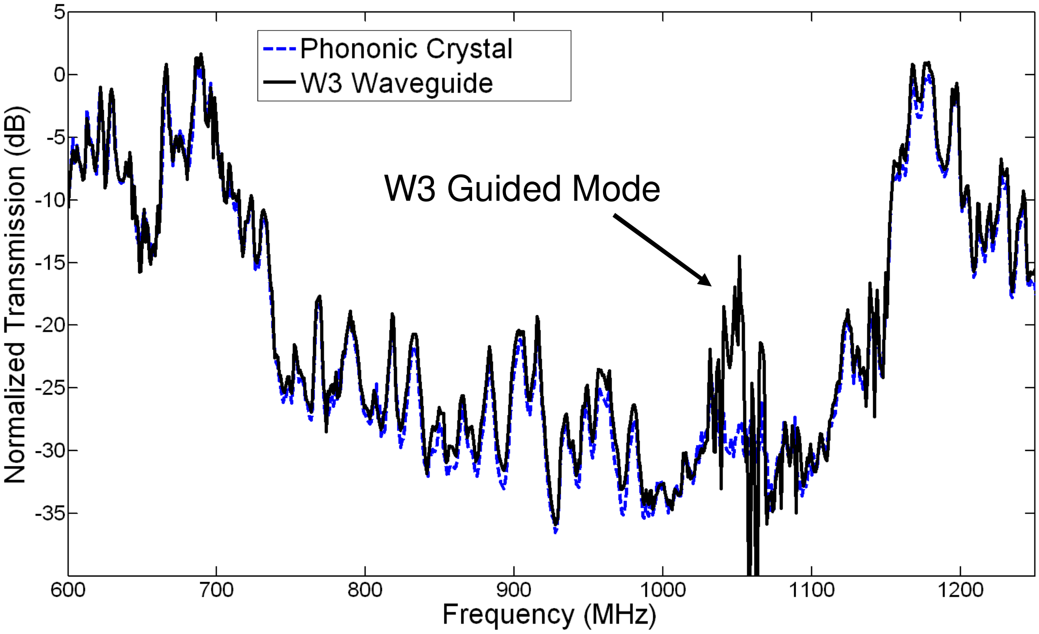

Figure 21. Measured response of the W3 waveguide in Figure 20. The strongest guided mode is between 1036 and 1055 MHz.

In order for phononic crystal devices to be widely applied in RF communications applications, the losses introduced by the devices must be negligible compared to that of the couplers, i.e. the normalized loss must approach 0 dB. This was the case for waveguides driven by slanted resonant couplers reported in [29]. In these devices, on one side of the coupler was the phononic crystal, on the other side was a slanted air/coupler interface. In such a design, if the acoustic signal is not coupled into the waveguide on the 1st pass, it is reflected by the crystal and the slanted air/coupler interface, where it is again incident on the waveguide or crystal. Given the high quality factors for SiO_2, W, Al and AlN in the VHF frequency range (> 1000), many passes at coupling into the waveguide are possible before the signal is damped. The phononic crystal waveguides reported here as well as the cavities reported in [38], both of which use a low reflecting coupler design (on one side of the coupler is the suspended phononic crystal, on the other side is a connection to the infinitely thick, lossy Si substrate), introduce significant additional loss. Such loss at an RF front-end will directly add to the noise figure of a receiver. Even in IF applications, additional gain and subsequent power consumption will be needed to overcome these losses. Further inspection of the W1 waveguide in Figure 18 reveals the likely source of loss for the UHF phononic crystal waveguides reported here. While the plane wave launched by the coupler has a width of approximately 98 μm, the W1 waveguide is only 4.7 μm wide at its narrowest width and is 5 μm wide at its opening. Thus, only about 5% of the power produced by the coupler is incident on the waveguide while the rest is reflected back toward the coupler by the phononic crystal. Small reflections at the interface between the coupler and suspended SiO_2 slab as well as reflections where the slab connects to the Si substrate, visible on the far right of Figure 15 A), may eventually couple more energy into the W1 waveguide, but it is unlikely that a design such as that in Figure 18 could reach a normalized (comparing to a 108 μm wide matrix) transmission of 0 dB. Reducing the width of the coupler is one option. This, however, will reduce the coupler response and increase coupler insertion loss. Furthermore, if the crystal is only a few periods wide, a two-dimensional phononic crystal can not be realized. The optimum solution would be to develop an acoustic focusing device or coupler, where acoustic energy can be focused with low loss into a W1 waveguide. Once the acoustic energy in concentrated in a narrow waveguide, cavities and other signal processing devices can be formed.

7 APPLICATIONS

Micro-phononic crystals are applicable to a number of existing micro-devices that manipulate acoustic energy and may serve as a tool for miniaturizing macro-acoustic components. Furthermore, new structures such as phononic-photonic crystals can enable interesting effects such as optical cooling [24]. Also suggested in [24] is the use of phononic crystals in thermal management and noise reduction through altering of the phonon density of states to modify thermal conductivity and heat capacity, but these applications are better addressed utilizing nano-scale phononic crystals yet to be developed. Outlined below are select examples where micro-scale phononic crystal devices can be applied to improve system and device performance in RF communications and acoustic imaging applications.

7.1 Acoustic Isolators

The micro-phononic crystals presented above are wide bandwidth, 2D acoustic mirrors that reflect up to 40 dB of the acoustic energy incident on the crystal. These properties make micro-phononic crystals useful for isolation of resonating structures such as coriolis force gyroscopes, micro-resonators, filters, and oscillators. One dimensional Bragg acoustic mirrors [39,40] are commonly used for the isolation of thin film AlN resonators that form the basis of cellular phone duplexers as depicted in Figure 22 (a). These duplexers isolate the narrowly separated transmit and receive frequencies in full-duplex CDMA cellular phones. Isolating a resonator from the substrate via a rigidly attached mirror rather than suspending it improves the power handling [39] and immunity to vibration. However, the ability of Bragg mirror stacks to isolate thin film resonators from the substrate is ultimately limited by their 1D nature and finite bandwidth. The reflection of incident acoustic energy is degraded for waves not propagating precisely in the direction of a 1D mirror. In a high Q resonator, even a small amount of off axis acoustic energy propagating though the mirror can limit the ultimate Q, or frequency selectivity, that can be achieved. Vibrating thin film resonators not only produce acoustic energy that is not normal to the substrate but also a small percentage of acoustic energy is converted into shear modes. Since the shear velocity is significantly lower than the longitudinal velocity, by 35% for both SiO_2 and W, the bandwidth of a 1D Bragg mirror is typically not wide enough to isolate both waves from the substrate. Since micro-phononic crystals are two and potentially three dimensional and have wide bandwidth, they can overcome the limited substrate isolation in 1D Bragg mirrors and ultimately provide resonators with higher-Q and filters with superior shape factor. A schematic of a thin film resonator isolated from the substrate by a 3D phononic crystal is shown in Figure 22 (b), where off axis and shear waves are reflected by the crystal. The wide bandwidth of micro-phononic crystals can also be utilized to isolate vibrating components operating over a large frequency range from the substrate, allowing single chip integration and close packing of many resonating devices.

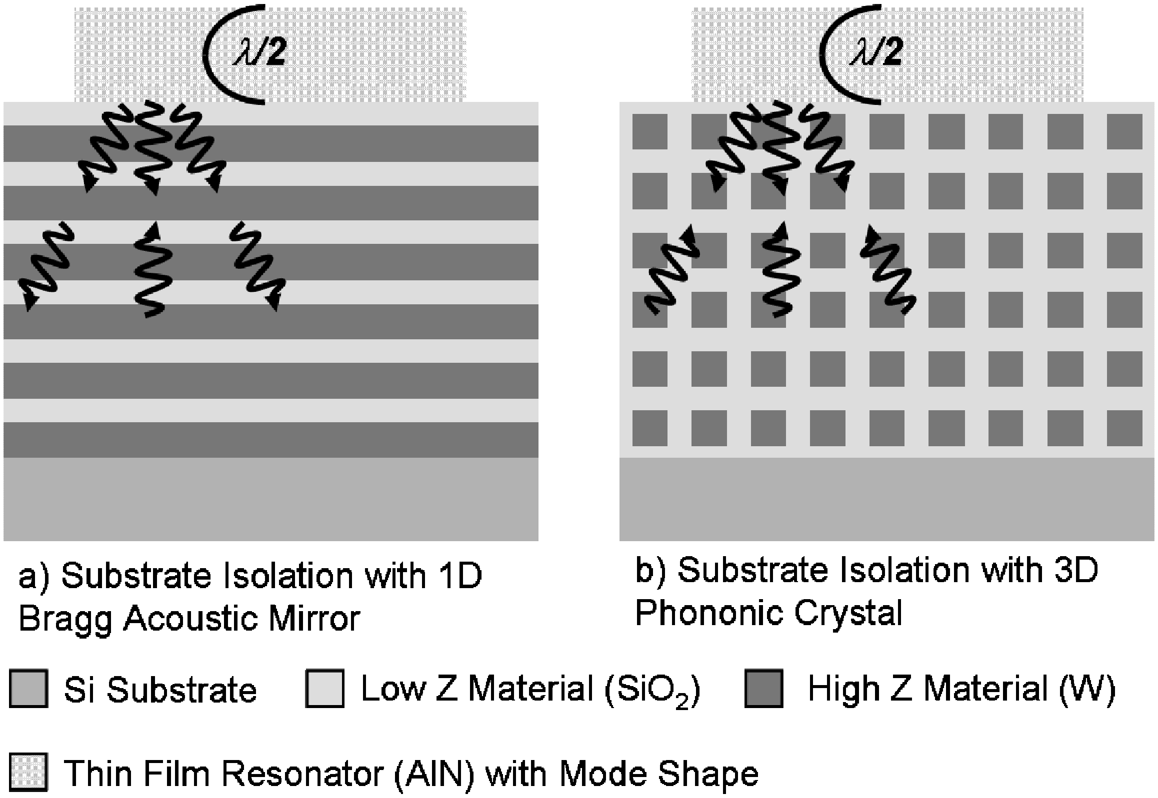

a) Substrate Isolation with 1D Bragg Acoustic Mirror

b) Substrate Isolation with 3D Phononic Crystal

Figure 22. (a) Substrate isolation of a thin film resonator using a 1D ¼ wavelength Bragg acoustic mirror stack. While very high reflectivity is obtained for longitudinal waves propagating in the direction of the mirror, the reflection of off axis and shear waves generated by the resonator is degraded, limiting substrate isolation and quality factor. (b) Substrate isolation of a thin film resonator using a 3D phononic crystal. The 3D nature of the crystal reflects incident acoustic waves at any angle and the bandgap covers a wide frequency range to reflect both longitudinal and shear waves.

7.2 Phononic Crystal Waveguides

Placing defects in a phononic crystal by removing scattering inclusions can be used to create waveguides that route and bend acoustic signals [13,14] as demonstrated above. Phononic crystal waveguides are useful for miniaturizing acoustic delay elements commonly used in signal processing and delay line oscillators. Delay line miniaturization is enabled by “slow sound”, the acoustic equivalent of the widely researched “slow light” in photonic crystals [41]. Both effects are induced by resonating of the wave as it propagates through the guide, slowing the group velocity by orders of magnitude with an equivalent reduction in size possible for a given time delay. Tapered waveguides can be used for miniaturized impedance matching, collimation and focusing in acoustic imaging applications such as medical ultrasound. Waveguiding can also be used to decouple the design of the transmitting/receiving element in an acoustic imaging system from the size of the aperture, or point from which the acoustic signal is emitted and collected. Generally, to obtain the highest resolution image, it is desirable to reduce as much as possible the size of the aperture for each element in an acoustic imaging array, allowing for a high density array of sensors. Unfortunately, the aperture size is typically limited by the electro-acoustic transduction element, where large size is required to achieve the high dynamic range necessary for deep acoustic imaging. Figure 23 shows a schematic depiction of how phononic crystal waveguides can be used to decouple the transducer from the aperture in acoustic imaging applications. In the figure, the signals from an array of large, high dynamic range capacitive micromachined ultrasonic transducers (cMUT) [42] (the use of piezoelectric transducer technology [43] is equally applicable here) are routed and focused to a group of small emitting points or apertures by a set of phononic crystal waveguides. The waveguiding operation is reversed in the return or sensing direction allowing for a more densely packed acoustic array capable of higher image resolution. The smaller aperture and more dense imaging array enhances or alleviates the need for creating synthetic apertures, a technique often employed to overcome image resolution problems in low density arrays.

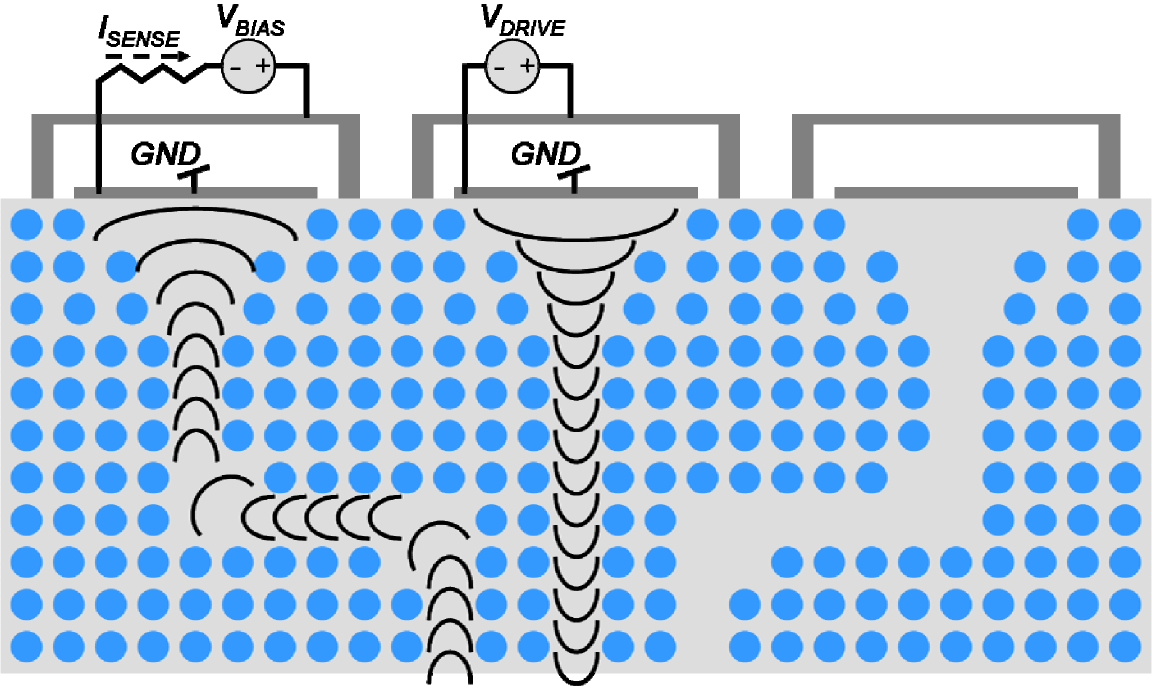

Figure 23. Schematic diagram depicting the use of phononic crystal waveguides to allow the acoustic signals from large electro-acoustic transducers to be emitted and detected through small apertures. Decoupling the transducer from the aperture enables higher density acoustic imaging which leads to higher image resolution.

7.3 Phononic Crystal Cavities and Filters

Perhaps the most compelling application of micro-phononic crystal technology is in the area of high-Q cavities and filters. Both series [15,16] and drop [17] cavities and filters have been demonstrated at the macro-scale in defected solid/water phononic crystals. Micro-phononic implementations of these cavities, schematically depicted in Figure 24 for 2D phononic crystal plates, not only pushes these devices to more relevant communications frequencies, but also allows for the cavities to be realized in high-Q solids, greatly improving the frequency selectivity and reducing the insertion loss. Shown in Figure 24 (a) is a phononic crystal point defect series resonant cavity. FDTD simulations of similar line defect cavities performed in our lab have demonstrated Qs approaching 10^4 for only 3 phononic crystal periods on each side of the cavity and normalized transmissions equal to 1. Efforts to demonstrate series cavities are ongoing. Figure 24 (b) demonstrates the coupling of two point defect series cavities to form a high order (4th in this case) filter. This form of coupling is potentially more repeatable, flexible and easier to manufacture than other forms of micro-scale mechanically-coupled resonator filters connected through small coupling beams [44].

Another advantage of phononic crystal based cavities and filters are the ability to decouple the high-Q resonator and electro-acoustic transducer design. State-of-the-art microresonator technology presents a trade-off between capacitive and piezoelectric based devices. Capacitive based microresonators implemented in high-Q materials such as Si, polycrystalline Si, and polycrystalline diamond have demonstrated record Q-frequency products of 2×10^{13} [44], but have high motional impedances associated with weak capacitive electro-acoustic transduction. The high resonator impedance leads to high filter insertion loss unless termination impedances greater than a few kΩ are employed. To reduce filter insertion loss and termination impedance many groups are now pursuing piezoelectric based microresonators [45-47] which have achieved sub-50 Ω motional impedances due to the orders of magnitude stronger electro-acoustic coupling. Unfortunately, the quality factors of these resonators are limited to a few thousand by the material losses in the piezoelectric layer and the metal electrodes required to transduce the devices. Phononic crystals allow micro-scale cavities (energy storage) to be realized in high-Q materials such as Si, SiO_2, and W while the electro-acoustic transduction is performed peripheral to the cavity using high efficiency piezoelectric couplers, overcoming the current Q, motional impedance trade-off in microresonator technology.

Figure 24 (c) and (d) depict drop and series/drop phononic crystal waveguide cavities reminiscent of distributed stripline resonators commonly used in microwave filters [48], where an acoustic implementation allows for miniaturization and higher Q. There are several interesting properties of these waveguide based filters. First, since phononic crystal waveguides are broadband compared to phononic crystal cavities, frequency division multiplexers and demultiplexers can be implemented by a waveguide and a series of cavities. Phononic crystal waveguide cavities can also be realized by changing the lattice constant in proximity to the waveguide. Waveguide cavities based on altering the crystal lattice constant or pitch with Qs of 10^6 [49] have been reported for photonic crystals. A significant advantage of this approach is the ability to set the cavity frequency based on pitch rather than an absolute dimension, as is the case in other micro-cavity technologies [39,40,43-47]. Pitch is much easier to control than a line dimension or film thickness, leading to much more precise setting of the cavity frequency and potentially eliminating the need for trimming.

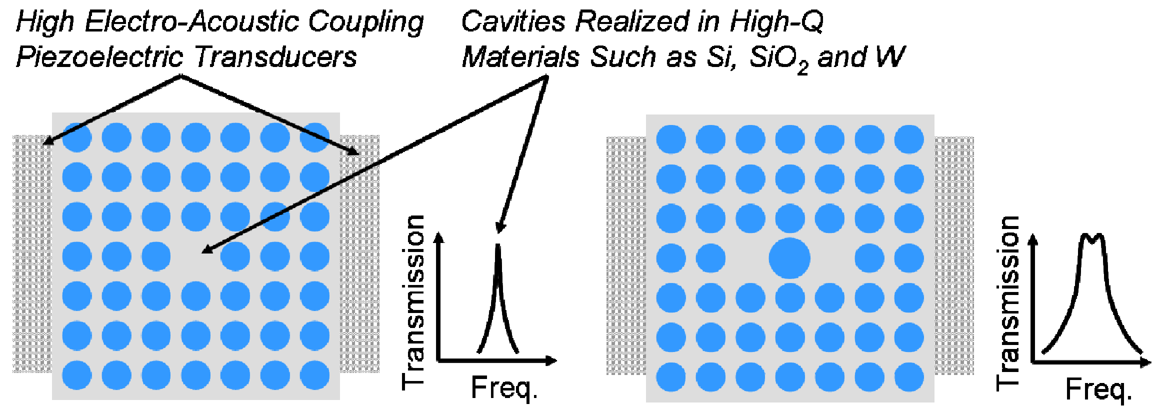

a) Series Cavity

b) Coupled Cavity Filter

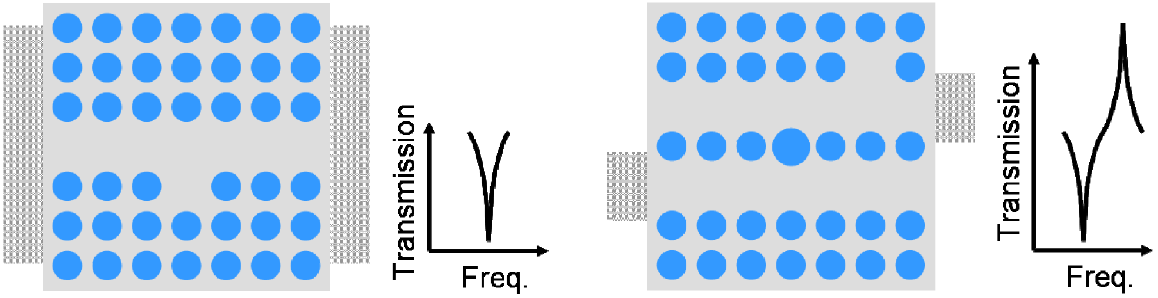

c) Drop Cavity in Waveguide

d) Waveguide Coupled Series and Drop Cavity Filter

Figure 24. Schematic diagram containing different types of cavities and filters that can be realized in a 2D defected phononic crystal plate. (a) Point defect series cavity, (b) two point defect series cavities coupled together to form a filter, (c) W1 waveguide with a drop cavity, and (d) two waveguides, one containing a drop cavity, coupled together by a series resonator. Decoupling of the resonant cavity and the electro-acoustic transducer shown in (a) allows the transducer to be realized in high coupling but moderate Q piezoelectric materials while the cavity is realized in high-Q phononic crystal materials. The waveguide filters in (c) and (d) enable distributed acoustic cavities and filters to be realized analogous to microstrip electromagnetic filters commonly used at microwave frequencies, where an acoustic implementation allows for miniaturization and higher frequency selectivity.

8 CONCLUSIONS

Microfabricated phononic crystals are an emerging research field that is poised to impact applications ranging from RF communications to medical ultrasound in the coming decade. Utilizing batch microfabrication we have demonstrated the 1st microscale phononic crystals in solid low loss materials, first at 67 MHz and later at nearly 1 GHz. Utilizing batch microfabrication allows direct integration of phononic crystals with piezoelectric transducers for rapid, low cost device interrogation. The integrated electro-acoustic interface along with the ability to defect a phononic crystal based on changes in a photolithographic mask enables the practical realization and use of micro-phononic crystal cavities, filters, and waveguides. Micro-scale phononic crystals have been demonstrated for high acoustic impedance W inclusions in a low acoustic impedance SiO_2 matrix. The advantages and disadvantages of different micro-scale phononic crystal architectures (cermet and network) and material sets (air/solid and solid/solid) have been compared and contrasted. Design techniques for realizing wide, deep phononic bandgaps based on Bragg and Mie resonant scattering, maximizing acoustic impedance mismatch, and optimizing velocity mismatch have been presented and discussed in the context of available materials and fabrication limits. The design and characterization of waveguides formed by removing rows of W inclusions from a W/SiO_2 phononic crystal plate have been reviewed. Application of micro-phononic crystal devices to wideband, multi-dimensional acoustic mirrors, high-Q, precisely manufactured cavities and filters, and the routing and focusing of acoustic imaging signals have been discussed. The reported advances reviewed in this report; batch micro-phononic crystal fabrication and simplified testing, promise not only the deployment of phononic crystals in a number of commercial applications but also far greater experimentation on a wide variety of phononic crystal structures than was previously possible.

9 METRICS

Publications and presentations:

R. H. Olsson III and I. El-Kady, "Microfabricated Phononic Crystal Devices and Applications," *Measurement Science and Technology,* 20 (2009) 012002 (13pp). ***(Invited Review)***

R. H. Olsson III, I. F. El-Kady, M. F. Su, M. R. Tuck, and J. G. Fleming, "Microfabricated VHF Acoustic Crystals and Waveguides," *Sensors and Actuators A: Physical,* vol. 145, pp. 87-93, July 2008.

I. El-Kady, R. H. Olsson III and J. G. Fleming, "Phononic Band-Gap Crystals for Radio Frequency Communications," *Applied Physics Letters,* 92, pp. 233504(1-3).

M. F. Su, R. H. Olsson III, Z. C. Leseman and I. El-Kady, "Realization of a Phononic Crystal Operating at Gigahertz Frequencies," *Applied Physics Letters,* In-Press.

R. H. Olsson III, I. El-Kady and M. R. Tuck, "Microscale Phononic Crystals and Devices," *EUROSENSORS 2008,* pp. 3-8, Sept. 2008. ***(Invited _Plenary)***

R. H. Olsson III, Y. Soliman, D. Goettler, M. Su, I. El-Kady, and Z Leseman, "Ultra High Frequency (UHF) Phononic Crystals Operating in Mobile Communication Bands," *IEEE Ultrasonics Symposium,* Sept. 2009, In-Press.

R. H. Olsson III, J. G. Fleming, I. F. El-Kady, M. R. Tuck, and F. B. McCormick, "Micromachined Bulk Wave Acoustic Bandgap Devices," *International Conf. on Solid-State Sensors, Actuators, and Microsystems,* pp. 317-321, June 2007.

J. G. Fleming, R. H. Olsson III, I. El-Kady, and M. Tuck, “CMOS Compatible, Electrically Transduced, Acoustic Bandgap Structures,” *International Symposium on Photonic and Electromagnetic Crystal Structures*, April 2007.

I. El-Kady, J. G. Fleming, R. H. Olsson III, and T. S. Luk, “Modeling of Micromachined Acoustic Bandgap Structures and Devices,” *International Symposium on Photonic and Electromagnetic Crystal Structures,* April 2007.

YM Soliman, DF Goettler, ZC Leseman, I El-Kady and RH Olsson III, *Effects of Release Hole Size on Microscale Phononic Crystals*, 10th Intl. Symp. On MEMS and Nanotech., SEM Ann. Conf., pp153, June 2009

R. H. Olsson IIII, “Piezoelectrically Transduced Microacoustic Devices for RF Communications and Sensing,” *DARPA Piezoelectric MEMS Workshop,* San Francisco, CA, March, 2008.

R. H. Olsson III, “Micro-Acoustic Devices for RF Communications and Sensing,” *Univ. of New Mexico Civil Engineering Graduate Seminar,* Albuquerque, NM, April, 2008.

R. H. Olsson III, “Micro-Acoustic Devices for RF Communication and Sensing,” *Marquette University Colloquium Series,* Milwaukee, WI, March, 2007.

Follow-on Programs:

Name	Funding Source	Duration	Description
Phonon Manipulation with Phononic Crystals	**LDRD**	**10/08-9/11**	**Research on Nano-Scale Phononic Crystals and Applications in Thermal Phonon Control**
Chip Scale Mechanical Spectrum Analyzers	**WFO DARPA**	**6/09-4/11**	**High-Q phononic crystal resonator arrays**

10 REFERENCES

[1] Montero de Espinosa F R, Jiménez E and Torres M 1998 Ultrasonic band gap in a periodic two-dimensional composite *Phys. Rev. Lett.* **80** 1208–11

[2] Sánchez-Pérez J V, Caballero D, Mártinez-Sala R, Rubio C, Sánchez-Dehesa J, Meseguer F, Llinares J and G’alvez F 1998 Sound attenuation by a two-dimensional array of rigid cylinders *Phys. Rev. Lett.* **80** 5325–8

[3] Robertson W M and Rudy J F III 1998 Measurement of acoustic stop bands in two dimensional periodic scattering arrays *J. Acoust. Soc. Am.* **104** Pt 1 694–9

[4] Miyashita T 2005 Sonic crystals and sonic wave-guides *Meas. Sci. Technol.* **16** R47-63

[5] Sigalas M M and García N 2000 Theoretical study of three dimensional elastic band gaps with the finite-difference time-domain method *J. Appl. Phys.* **87** 6 3122-5

[6] Kee C-S, Kim J-E, Park H Y, Chang K J and Lim H 2000 Essential role of impedance in the formation of acoustic band gaps *J. Appl. Phys.* **87** 4 1593-6

[7] Kafesaki M and Economou E N 1999 Multiple-scattering theory for three-dimensional periodic acoustic composites *Phys. Rev. B* **60** 17 11993-2001

[8] Hsu J-C and Wu T-T 2006 Bleustein-Gulyaev-Shimizu surface acoustic waves in two-dimensional piezoelectric phononic crystals *IEEE Trans. Ultrasonics, Ferroelectrics and Freq. Cont.* **53** 6 1169-76

[9] Vasseur J O, Deymier P A, Chenni B, Djafari-Rouhani B, Dobrzynski L and Prevost D 2001 Experimental and theoretical evidence for the existence of absolute acoustic band gaps in two-dimensional solid phononic crystals *Phys. Rev. Lett.* **86** 14 3012-5

[10] Hsiao F, Khelif A, Moubchir H, Choujaa A, Chen C and Laude V 2007 Complete band gaps and deaf bands of triangular and honeycomb water-steel phononic crystals, *J. Appl. Phys.,* **101** 044903

[11] Yang S, Page J H, Liu Z, Cowan M L, Chan C T and Sheng P 2002 Ultrasound tunneling through 3D phononic crystals *Phy. Rev. Lett.* **88** 10 104301

[12] Vasseur J O, Hladky-Hennion A-C, Djafari-Rouhani B, Duval F, Dubus B, Pennec Y and Deymier P A 2007 Waveguiding in two-dimensional piezoelectric phononic crystal plates *J. Appl. Phys.* **101** 114904

[13] Khelif A, Choujaa A, Benchabane S, Djafari-Rouhani B and Laude V 2004 Guiding and bending acoustic waves in highly confined phononic crystal waveguides *Appl. Phys. Lett.* **84** 22 4400-2

[14] Torres M, Montero de Espinosa F R and Aragón J L 2001 Ultrasonic wedges for elastic wave bending and splitting without requiring a full band gap *Phys. Rev. Lett.* **86** 4282–5

[15] Khelif A, Choujaa A, Djafari-Rouhani B, Wilm W, Ballandras S and Laude V 2003 Trapping and guiding of acoustic waves by defect modes in a full-band-gap ultrasonic crystal *Phys. Rev. B* **68** 214301

[16] Khelif A, Deymier P A, Djafari-Rouhani B, Vasseur J O and Dobrzynski L 2003 Two-dimensional phononic crystal with tunable narrow pass band: Application to a waveguide with selective frequency *J. Appl. Phys.* **94** 3 1308-11

[17] Benchabane S, Khelif A, Choujaa A, Djafari-Rouhani B and Laude V 2005 Interaction of waveguide and localized modes in a phononic crystal *Europhys. Lett.* **71** 4 570-5

[18] Van Der Biest F, Sukhovich A, Tourin A, Page J H, van Tiggelen B A, Liu Z and Fink M 2005 Resonant tunneling of acoustic waves through a double barrier consisting of two phononic crystals *Europhys. Lett.* **71** 1 63

[19] Shi J, Lin S and Huang T J 2008 Wide-band acoustic collimating by phononic crystal composites *Appl. Phys. Lett.* **92** 111901

[20] Yang S, Page J H, Liu Z, Cowan M L Chan C T and Sheng P 2004 Focusing of sound in a 3D phononic crystal *Phys. Rev. Lett.* **93** 2 024301

[21] Zhang X and Liu Z 2004 Negative refraction of acoustic waves in two-dimensional phononic crystals *Appl. Phys. Lett.* **85** 2 341-3

[22] Ke M, Liu Z, Qiu C, Wang W, Shi J, Wen W and Sheng P 2005 Negative-refraction imaging with two-dimensional phononic crystals *Phys. Rev. B* **72** 064306

[23] Dahr L and Rogers J A 2000 High frequency one-dimensional phononic crystal characterized with a picosecond transient grating photoacoustic technique *Appl. Phys. Lett.* **77** 9 1402-4

[24] Gorishnyy T, Ullal C K, Maldovan M, Fytas G and Thomas E L 2005 Hypersonic phononic crystals *Phys. Rev. Lett.* **94** 115501

[25] Cheng W, Wang J, Jonas U, Fytas G and Stephanou N 2006 Observation and tuning of hypersonic bandgaps in colloidal crystals *Nature Materials* **5** 830-6

[26] Wu T, Wu L and Huang Z 2005 Frequency band-gap measurement of two-dimensional air/silicon phononic crystals using layered slanted finger interdigital transducers *J. Appl. Phys.* **97** 094916

[27] Benchabane S, Khelif A, Rauch J-Y, Robert L and Laude V 2006 Evidence for complete surface wave band gap in a piezoelectric phononic crystal *Phys. Rev. E* **73** 065601(R)

[28] Olsson III R H, Fleming J G, El-Kady I F, Tuck M R and McCormick F B 2007 Micromachined bulk wave acoustic bandgap devices *Tech. Dig. Int. Conf. on Solid-State Sensors, Actuators, and Microsystems* (Lyon) 317-21

[29] Olsson III R H, El-Kady I F, Su M F, Tuck M R and Fleming J G 2007 Microfabricated VHF acoustic crystals and waveguides *Sensors and Actuators A: Physical* doi:10.1016/j.sna.2007.10.081

[30] El-Kady I, Olsson III R H and Fleming J G 2008 Phononic band-gap crystals for RF communications *Appl. Phys. Lett.* doi:10.1063/1.2938863

[31] Olsson III R H, Su M F, Griego S X, Soliman Y, Goettler D, El-Kady I, and Leseman Z 2009 Ultra high frequency (UHF) phononic crystals operating in mobile communication bands *IEEE Ultrasonics Symposium* In-Press

[32] El-Kady I and Olsson III R H 2008 Physical origins of deep wide phononic bandgaps *Phys. Rev. E* - in review

[33] Economou E N and Sigalas M 1993 *Photonic Band Gaps and Localization (NATO Advanced Science Institutes Series, Series B: Physics* vol 308) ed C M Soukoulis (New York: Plenum Press) pp 317-38

[34] Mohammadi S, Eftekhar A A, Khelif A, Moubchir H, Westafer R, Hunt W D and Adibi A 2007 Complete phononic bandgap maps in two-dimensional silicon phononic crystal plates *Elect. Lett.* **43** 16 898-9

[35] Mohammadi S, Eftekhar A A, Khelif A, Hunt W D and Adibi A 2008 Evidence of large high-frequency complete phononic band gaps in silicon phononic crystal plates *Appl. Phys. Lett.* - in press

[36] Tse S W H, Karousos A and Young P R (2004) Broadband photonic bandgap waveguides *IEEE MTT-S Int. Microwave Symp. Dig.* (Fort Worth) 2063-66

[37] Olsson III R H and El-Kady I 2009 Microfabricated phononic crystal devices and applications *Measurement Science and Technology,* **20** 012002 13pp

[38] Mohammadi S, Eftekhar A A, Hunt W D, and Adibi A 2009 High-Q Micro-Mechanical Resonators in Two-Dimensional Phononic Crystal Slab *Appl. Phys. Lett.* **94** 051906

[39] Aigner R 2004 Volume manufacturing of BAW-filters in a CMOS fab *Tech. Dig. 2nd Int. Symp. On Acoustic Dev. for Future Mobile Comm. Sys.* (Chiba) 129-34

[40] Lakin K M 2005 Thin film resonator technology *IEEE Trans. on Ultrasonics, Ferroelectrics, and Freq. Cont.* **52** 5 707-16

[41] Krauss T F 2007 Slow light in photonic crystal waveguides *J. Phys. D: Appl. Phys.* **40** 2666-70

[42] Buhrdorf A, Ahrens O and Binder J 2001 Capacitive micromachined ultrasonic transducers and their application *Proc. IEEE Ultrasonics Symp.* (Atlanta) 933-40

[43] Shung K K and Zipparo M 1996 Ultrasonic transducers and arrays *IEEE Eng. in Med. and Bio. Mag.* **15** 6 20-30

[44] Nguyen C T-C 2007 MEMS technology for timing and frequency control *IEEE Trans. on Ultrasonics, Ferroelectrics, and Freq. Cont.* **54** 2 251-70

[45] Piazza G, Stephanou P J and Pisano A P 2007 Single-chip multiple frequency AlN MEMS filters based on contour-mode piezoelectric resonators *J. of Microelectromechanical Sys.* **16** 2 319-28

[46] Olsson III R H, Fleming J G, Wojciechowski K E, Baker M S and Tuck M R 2007 Post-CMOS compatible aluminum nitride MEMS filters and resonant sensors *Proc. IEEE Freq. Cont. Symp.* (Geneva) 412-9

[47] Pan W, Abdolvand R and Ayazi F 2008 A low-loss 1.8GHz monolithic thin-film piezoelectric-on-substrate filter *Proc. IEEE Conf. on Microelectromechanical Sys.* (Tucson) 176-9

[48] Pozar D M 1998 *Microwave Engineering* (New York: John Wiley and Sons)

[49] Asano T, Song B-S, Akahane Y and Noda S 2006 Ultrahigh-Q nanocavities in two-dimensional photonic crystal slabs *IEEE J. of Selected Topics in Quantum Elect.* **12** 6 1123-34

Distribution

1	MS0123	D. Chavez, LDRD Office	1011 (electronic copy)
1	MS1069	Roy H. Olsson III	1749-2 (electronic copy)
1	MS1082	Frederick McCormick	1727 (electronic copy)
1	MS1082	Ihab El-Kady	1725 (electronic copy)
1	MS1080	Keith Ortiz	1749 (electronic copy)
1	MS0899	Technical Library	9536 (electronic copy)

Sandia National Laboratories